Changes in elevation and mass of Arctic glaciers and ice caps, 2010-2017

P. Tepes[1], N. Gourmelen[1,2], P. Nienow[1], M. Tsamados[3], A. Shepherd[4], and F. Weissgerber[1]

[1]School of GeoSciences, University of Edinburgh, UK.
[2]IPGS UMR 7516, Université de Strasbourg, CNRS, Strasbourg, France.
[3]Centre for Polar Observation and Modeling, University College London, London, UK.
[4]Centre for Polar Observation and Modelling, School of Earth and Environment, University of Leeds, Leeds, UK.

Corresponding author: Paul Tepes (paul.tepes@ed.ac.uk)

Key words:

- Arctic glaciers and ice caps
- Mass balance
- Arctic warming
- CryoSat-2
- Swath processing

Abstract

Arctic glaciers and ice caps (GIC) are losing mass rapidly, and this process is expected to continue during the 21st century owing to polar amplification of climate warming. Here, we use seven years of CryoSat-2 swath interferometric altimetry to track changes in the volume of Arctic GIC. From these data, we produce a pan-Arctic assessment of GIC mass imbalance, and we partition their losses into signals associated with atmospheric processes and glacier dynamics. Between 2010 and 2017, Arctic GIC lost 609 ± 7 Gt of ice, contributing 0.240 ± 0.007 millimetres per year to global sea level rise. While surface ablation is responsible for 87 % of losses across the Arctic, dynamic imbalance is increasing in the Barents and Kara Sea region where it now accounts for 43 % of total ice loss. Arctic GIC's dynamic imbalance is associated with a northward shift of Atlantic climate, and this effect should be considered in global sea level projections.

1. Introduction

Arctic glaciers and ice caps (GIC) are key players in the local freshwater budget, impact thermohaline forcing in the North Atlantic (Thornalley et al., 2018; Yang et al., 2016), and are significant contributors to global eustatic sea level rise (Ciracì et al., 2020; Gardner et al., 2013; Zemp et al., 2019). They store 40 % of the global GIC ice volume, equating to 144 mm of sea level equivalent (Farinotti et al., 2019), and their losses are currently increasing as atmospheric and oceanic forcing intensify (Barton et al., 2018; Ding et al., 2014) and as Arctic sea ice cover shrinks (Onarheim et al., 2018). Furthermore, the dynamic response of land ice to climate forcing constitutes the main uncertainty in global sea level projections for the next century (Church, 2013; Martin and Adcroft, 2010). To address this knowledge gap, observations of the relative contribution of both surface mass balance (SMB) and ice dynamics (D) to the total losses are necessary. A recent study finds that between 1972 and 2018, D accounted for 66 % of the total

mass imbalance of the Greenland Ice Sheet (Mouginot et al., 2019). For the GIC of the Arctic however, the SMB-to-D ratio is unknown.

SMB is determined by thermodynamic processes at the ice surface, and is modified by shifts in large-scale atmospheric circulation patterns (Delhasse et al., 2018) and by CO_2-induced radiative forcing (Byrne and Schneider, 2018; Shindell and Faluvegi, 2009). In addition to negative overall SMB, the Arctic GIC mass imbalance was amplified in recent years by the large-scale destabilisation of marine-terminating drainage basins, during which ice flow and thus flux to the ocean was locally increased by several orders of magnitude (Haga et al., 2020; McMillan et al., 2014; Nuth et al., 2019; Strozzi et al., 2017a; Willis et al., 2018). The persistent incursion of warm North Atlantic Ocean water into the Arctic Ocean is thought to have direct impact on sea ice extent and tidewater glacier dynamics (Barton et al., 2018; McMillan et al., 2014; Polyakov et al., 2017). The respective role of internal processes, commonly ascribed to glacier surges, and external climatic forcing in driving these dynamic instabilities remains largely unclear (Dunse et al., 2015; McMillan et al., 2014). The relative impact of atmospheric and oceanic influences on glacier fluctuations at the ice-ocean interface is also uncertain, with potential control from both oceanic heat transport and surface runoff (Cowton et al., 2018). Here, we use CryoSat-2 swath interferometric altimetry (Foresta et al., 2016; Gourmelen et al., 2018) to measure changes in the volume of Arctic GIC with unprecedented spatial resolution and to partition the observed changes into signals associated with atmospheric processes, via SMB, and glacier dynamics.

2. Pan-arctic view of GIC thinning

We derive rates of change in land ice surface elevation $\dot{h}$ in all areas of the Arctic beyond Greenland. This includes the southern and northern Canadian Arctic Archipelagos (CAA-S and CAA-N, respectively), Iceland (Ic), Svalbard (Sv), and the Russian Arctic Archipelagos (RAA) of Franz Josef Land (FJL), Novaya Zemlya (NZ) and Severnaya Zemlya (SZ) (Fig. 1). We apply

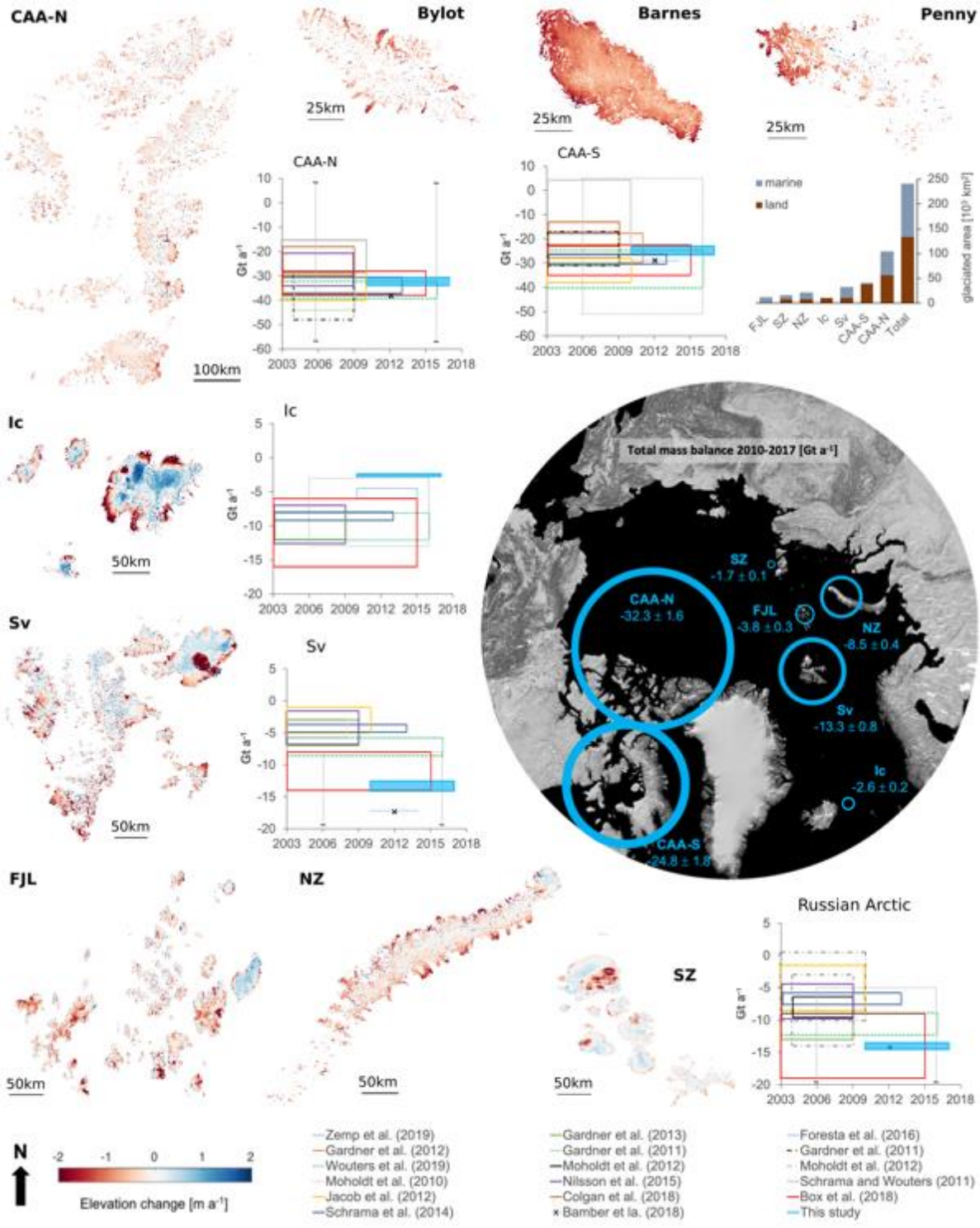

Fig. 1. Rates of $\dot{h}$ (expanded maps available in Appendices C1-C6), glaciated area of marine- and land-terminating glacier catchments, and Arctic GIC mass balance represented in graphical form as boxes indicating average values over their respective study period (width) with error estimates (height). A map of the Arctic shows the location of GIC and mass balance from the present study represented by circles with size proportional to the mass losses and their width proportional to the error budget.

swath processing to CryoSat-2 altimetry data spanning the period 2010-2017 to retrieve time-dependent elevation measurements over the GIC (Gourmelen et al., 2018). The high density of observations enables us to compute mean $\dot{h}$ over unit areas of 500 by 500 m to ensure sufficient spatial detail while maximising the number of observations in each resolution cell (Foresta et al., 2016) (Appendix A1-A3). Regionally, this translates into a ratio of measured-to-total glaciated area equal to 83 % over the GIC of the Russian Arctic, 79 % over Svalbard and Iceland, and 60 % over the Canadian Arctic, with good coverage over the ice margins (Appendices B and C).

Ice thinning is widespread across the Arctic, and the median rate of elevation change is -0.25 m a^{-1}. There is, however, considerable spatial variability, and the 5 % and 95 % quantiles are -1.65 m a^{-1} and +0.70 m a^{-1} respectively, reflecting the diversity of responses of ice masses to forcing across the Arctic (Fig. 1).

The climate of the southern and northern Canadian Arctic Archipelagos exhibits low inter-annual variability in precipitation but high variability in summer surface temperatures (Gardner et al., 2012), which results in spatially homogeneous thinning patterns, driven largely by changes in summer surface melt rates (Gardner et al., 2012, 2011). Median thinning rates over CAA-S (0.75 m a^{-1}) are three times larger than over CAA-N (0.24 m a^{-1}), reflecting the latitudinal control on SMB. Rates of thinning of up to 5 m a^{-1} are observed at low elevations and over a limited number of marine-terminating outlet glaciers, including on Devon Ice Cap and Prince of Wales Icefield (Appendices C6a,c,e). The strongest spatially extensive thinning signal across CAA-S is from the ablation zone of Barnes and Penny Ice Caps where thinning rates are in excess of 2.5 m a^{-1} (Fig. 1 and Appendix C6b). Icelandic ice caps display diverse patterns of glacier change (Fig. 1), reflecting in part their location over volcanically active terrain, frequent surges, and high variability in climate patterns (Foresta et al., 2016). Nevertheless, between 2010 and 2017, they have mainly experienced SMB-driven elevation changes, with strong seasonal trends and high melt rates of up to 6 m a^{-1} along ice cap margins, and thickening in the accumulation zones driven by post-

surge dynamic responses and exceptionally large winter accumulation in recent years (Foresta et al., 2016; Wouters et al., 2019).

Complex patterns of change also prevail over the archipelagos of the Barents and Kara Sea (BKS) region, which include both Svalbard and the Russian Arctic Archipelagos, where rates of $\dot{h}$ have high spatial variability (Fig. 1). Pronounced thinning (> 1 m a^{-1}) is observed at a large number of tidewater glaciers, with marine-terminating basins representing in total 66 % of the glaciated area across the BKS region. Examples of increased thinning associated with dynamic change include an increasing number of marine-terminating basins in Svalbard, such as along the southeastern flanks of Austfonna Ice Cap, including Basin 3 (McMillan et al., 2014), and the frontal destabilisation of Stonebreen, Edgeøya (Strozzi et al., 2017a). In Severnaya Zemlya, six basins are thinning at an average rate (0.85 m a^{-1}) an order of magnitude higher than the rest of the archipelago (0.08 m a^{-1}); all six of these are marine-terminating catchments located primarily around the southern and eastern flanks of the Academy of Sciences Ice Cap (Moholdt et al., 2012a; Sánchez-Gámez et al., 2019), with one on the western flank of Vavilov Ice Cap (Willis et al., 2018) (Appendix C4). Fed by ice streams from the Karpinsky and Rusanov Ice Caps (Appendix C4), the collapse of the Matusevich Ice Shelf in 2012 triggered the rapid acceleration of two main outlet glaciers of Karpinsky Ice Cap, one having sped up by up to 200 % at its terminus between 2010 and 2014 (Willis et al., 2015). Windy Ice Cap on Graham Bell Island, the easternmost ice cap in Franz Josef Land (Appendix C2), represents a singularity in the archipelago, thickening at an average rate of 0.4 m a^{-1}, thereby maintaining a positive trend since the 1950s (Moholdt et al., 2012b; Zheng et al., 2018).

3. Arctic GIC mass balance

We convert elevation to volume change using glacier area extents from the Randolph Glacier Inventory (RGI 6.0) and we derive mass budgets (Appendices A5-A7) using an assumed constant

density of ice ρ_{ice} equal to 850 ± 60 kg m^{-3} (Huss, 2013) (Table 1). Between 2010 and 2017, Arctic GIC outside of Greenland lost on average 87.0 ± 2.6 Gt of ice per year (Fig. 1, Table 1), corresponding to a mean sea level contribution of +0.240 ± 0.007 mm a^{-1}. The largest losses occurred over the Canadian Arctic, with mass trends of -32.3 ± 1.6 Gt a^{-1} and -24.8 ± 1.8 Gt a^{-1} for CAA-N and CAA-S, respectively. The largest loss per unit area is for CAA-S (606 ± 44 kg m^{-2} a^{-1}), followed by Svalbard (401 ± 24 kg m^{-2} a^{-1}), Novaya Zemlya (385 ± 18 kg m^{-2} a^{-1}), CAA-N (308 ± 15 kg m^{-2} a^{-1}), Franz Josef Land (297 ± 23 kg m^{-2} a^{-1}), and Iceland (234 ± 18 kg m^{-2} a^{-1}). Specific mass loss over Severnaya Zemlya (-106 ± 6 kg m^{-2} a^{-1}) is the lowest in the Arctic, representing ~1/4 of the rate of loss over Novaya Zemlya and ~1/3 that of Franz Josef Land.

Table 1
Summary table of mass budget: total mass balance and cumulative contributions to sea level rise (SLR) of Arctic GIC from 2010 to 2017.

Region	Total area* [10^3 km^2]	Mass budget** [Gt a^{-1}] 2003-2009	Mass budget*** [Gt a^{-1}] 2010-2017	Mass budget [kg m^{-2} a^{-1}] 2010-2017	SLR [mm a^{-1}] 2010-2017
FJL	12.8	-0.6 ± 0.9	-3.8 (-4.0) ± 0.3	-297 ± 23	+0.010 ± 0.001
NZ	22.1	-7.1 ± 1.2	-8.5 (-9.0) ± 0.4	-385 ± 18	+0.024 ± 0.001
SZ	16.0	-1.4 ± 0.9	-1.7 (-1.8) ± 0.1	-106 ± 6	+0.005 ± 0.000
Sv	33.2	-5 ± 2	-13.3 (-14.1) ± 0.8	-401 ± 24	+0.037 ± 0.002
Ic	11.1	-10 ± 2	-2.6 (-2.8) ± 0.2	-234 ± 18	+0.007 ± 0.001
CAA-N	105.0	-33 ± 4	-32.3 (-34.2) ± 1.6	-308 ± 15	+0.089 ± 0.004
CAA-S	40.9	-27 ± 4	-24.8 (-26.3) ± 1.8	-606 ± 44	+0.068 ± 0.005
RAA	50.9	-11 ± 4	-14.0 (-14.8) ± 0.5	-275 ± 10	+0.039 ± 0.001
BKS	84.1	-16 ± 4	-27.3 (-28.9) ± 0.9	-325 ± 11	+0.075 ± 0.002
CAA	145.9	-60 ± 6	-57.1 (-60.5) ± 2.4	-391 ± 16	+0.186 ± 0.008
Total Arctic	**241.1**	**-86 ± 7**	**-87.0 (-92.1) ± 2.6**	**-361 ± 11**	**+0.240 ± 0.007**

* Total glaciated area (RGI 6.0), ** mass budgets using a constant density of ice equal to 900 kg m^{-3} (Gardner et al., 2013) for RAA, Sv, Ic, CAA-N and CAA-S, and (Moholdt et al., 2012b) for NZ, SZ and FJL, which cover the period 2004–2009), *** mass budgets using a constant density of ice at 850 kg m^{-3} (900 kg m^{-3} for comparison with the 2003-2009 mass budget estimates).

Our measurements reveal an increase in mean annual ice loss of 7 % between the 2003-2009 ICESat period (Gardner et al., 2013) and our 2010-2017 study period. However, this overall mass loss hides contrasting patterns of change across the regions. While during 2010-2017, the

Canadian Arctic has seen a rate of loss comparable to the period between 2003 and 2009 (Table 1), Icelandic glaciers have lost mass at a lower rate, due primarily to recent high rates of winter accumulation leading locally to positive SMB (Foresta et al., 2016; Wouters et al., 2019). The largest increase in rates of mass loss occurred within the BKS sector. Rates of ice loss over Svalbard, for example, almost trebled over the CryoSat-2 measurement period (13.3 ± 0.8 Gt a^{-1}) compared to the previous six years (Table 1). In the Russian Arctic, Franz Josef Land went from near-balance conditions during the 2004-2009 period (0.6 ± 0.9 Gt a^{-1}) to considerable mass loss during 2010-2017 (3.8 ± 0.3 Gt a^{-1}) (Table 1), and up to 4.4 ± 0.8 Gt a^{-1} during 2011-2016 (Zheng et al., 2018). Novaya Zemlya remained the largest contributor to sea level change in the Russian Arctic, losing 8.5 ± 0.4 Gt a^{-1} between 2010 and 2017. This is 27 % more ice loss per year compared to 2004-2009 (Moholdt et al., 2012b), and 80 % more than the 60-year average (5.1 ± 0.8 Gt a^{-1}) (Melkonian et al., 2016). Our mass balance estimate for Novaya Zemlya matches the 2012-2013/14 rate (-8.5 Gt a^{-1}) from WorldView stereo-pair imagery (Melkonian et al., 2016), and is similar to a longer-term (2002-2016) mean of -8 ± 4 Gt a^{-1} derived from a combination of IceSat, GRACE and CryoSat-2 measurements (Ciracì et al., 2018). It is however lower, although within error, compared with Ciracì et al.'s 2010-2016 estimate (-13.3 ± 5 Gt a^{-1}) using conventional CryoSat-2 point-of-closest-approach processing (Ciracì et al., 2018). Severnaya Zemlya's rate of loss was 29 % higher compared to the previous decade, reaching 1.7 ± 0.1 Gt a^{-1} in 2010-2017 (Table 1). Overall, GIC within the BKS sector have released an extra 100 km^3 of freshwater to the ocean between 2010 and 2017 compared to the previous decade, a volume similar in magnitude to that associated with receding sea ice cover in this region (Labe et al., 2018; Onarheim et al., 2018).

4. Surface mass balance and glacier dynamics

Over land-terminating GIC, elevation change rates $\dot{h}$ can be related directly to the local SMB anomaly (Fig. 2a). It is thereby assumed that surface processes dominate the mass loss, and dynamic thickness changes resulting from glacier surges are either negligible, or cancel out across the entire area A_l of land-terminating basins, such that $\dot{h}_l \approx SMB_l/(A_l * \rho_{ice})$. To quantify the relative contribution of SMB and D to the overall mass loss for each of the seven regions listed in Table 1, we first parametrise elevation change $\dot{h}_l$ over land-terminating GIC as a function of first-order controls on SMB_l, that is elevation (h_l), and spatial coordinates (x_l, y_l) :

$$\dot{h_l} \approx a_0 {h_l}^3 + a_1 {h_l}^2 + a_2 h_l + a_3 x_l + a_4 y_l + a_5$$

We then use our parametrisation to *i)* estimate bulk SMB_m over marine-terminating sectors, and *ii)* derive a bulk loss of D by subtracting SMB_m from the total marine-terminating GIC mass balance (Appendix A8). A comparison between our derived SMB and that of the regional atmospheric climate model RACMO2.3 over land-terminating GIC in the Canadian Arctic (Noël et al., 2018) demonstrates an excellent agreement (Fig. 2b, Appendix A9). It also highlights the ability of our parametrisation to capture the first order SMB dependency on elevation and geographical location resulting in SMB variability between land- and adjacent marine-terminating sectors (Fig. 2a,c). Fig. 2c illustrates the spatial distribution of the partitioning after extracting the SMB_m signal over marine-terminating basins across two regions where dynamic thinning has been a key mechanism of ice loss during the 2010s, namely Austfonna Ice Cap (Dunse et al., 2015) and Severnaya Zemlya (Sánchez-Gámez et al., 2019; Zheng et al., 2019).

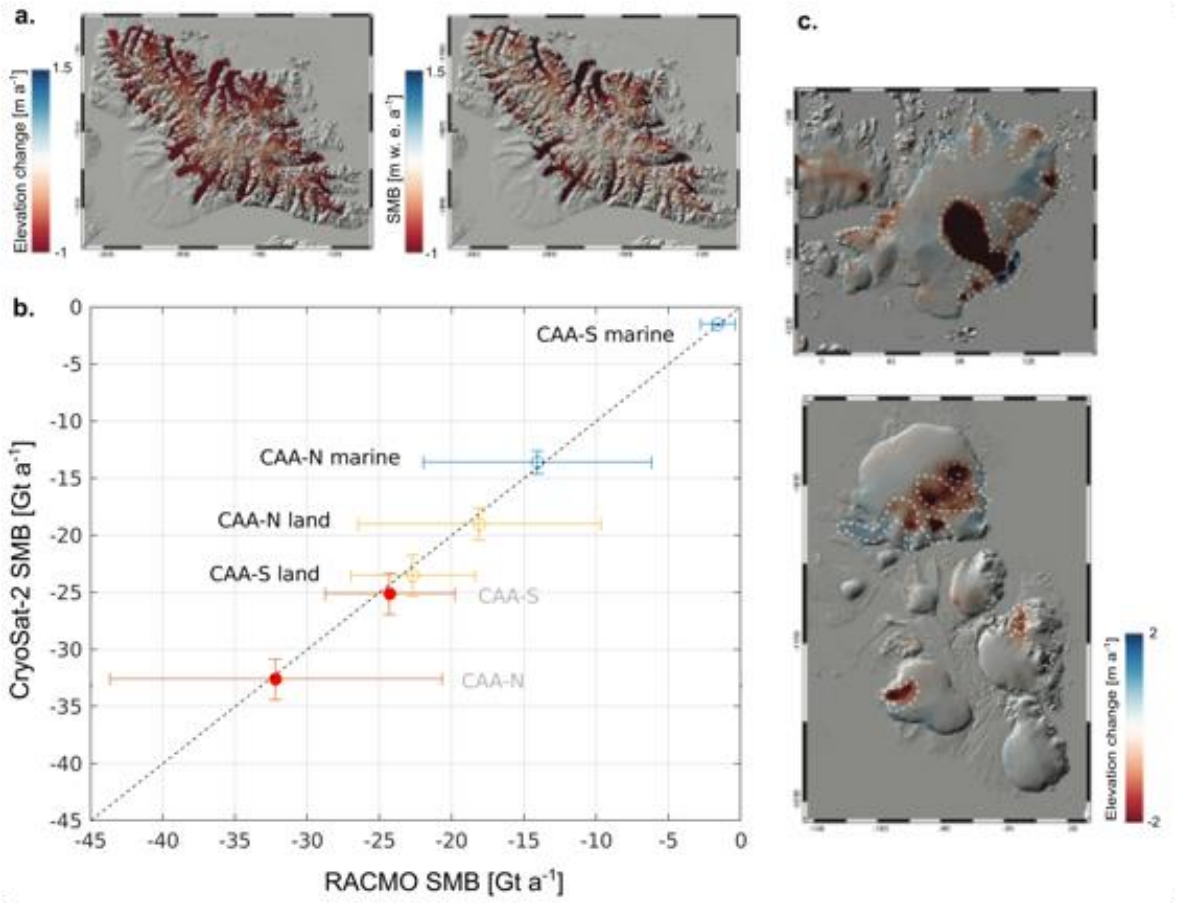

Fig. 2. a. CryoSat-2 derived $\dot{h}$ (left) *versus* RACMO2.3 SMB (right) over Bylot Island, CAA-S; **b.** SMB from CryoSat-2 *versus* RACMO2.3 across the Canadian Arctic: all regions (red), land-terminating sectors (yellow), marine-terminating sectors (blue); **c.** dynamic thinning $\dot{h} - \dot{h}_{p_m}$ (Appendix A8) over major BKS flow units: Austfonna Ice Cap (upper panel) and Severnaya Zemlya archipelago (lower panel). The white dashed lines demarcate areas of dynamic thinning.

We observe an increasingly negative area-specific SMB with distance from the pole over the Canadian Arctic (Fig. 3). In contrast, a simple latitudinal control on SMB is not apparent across the archipelagos east of Greenland, reflecting the more complex interplay between atmospheric and oceanic influences. Noteworthy are the Sv-FJL-SZ and NZ-SZ gradients of SMB, with less negative values in a north-eastward direction resulting from decreasing incursions of hot, moist Atlantic air masses (Moholdt et al., 2012b). Finally, our results confirm that SMB dominates the total mass budget west of Greenland, with near-zero contribution from D. According to Millan et al. (2017), this contribution has been decreasing since the early 1990s, attaining 3 - 4 Gt a^{-1} during

2010-2015, and driven by discharge from a very small number of catchments. For example, in 2015, two single glacier basins (Trinity and Wykeham on Prince of Wales Ice Cap, Appendix C6e) accounted for 50 % of the total ice discharge in the CAA (Millan et al., 2017).

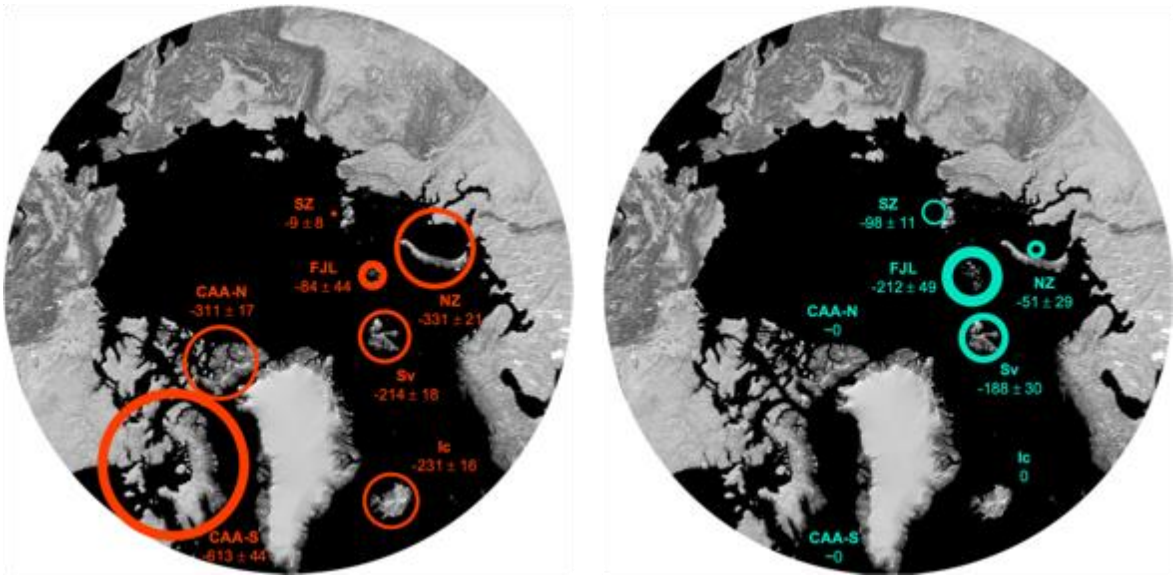

Fig. 3. Area-specific mass balance in [kg m^{-2} a^{-1}]: SMB (orange, left) and D (cyan, right), derived from CryoSat-2. Circles with size proportional to ice mass losses and their width proportional to the corresponding error budget.

At the pan-Arctic scale, the regional differences in the dynamic component D contrast significantly with SMB, with a pronounced and strong imbalance in the BKS region compared with the rest of the Arctic (Fig. 3). Between 2010 and 2017, ice losses in the BKS sector were nearly two times larger per unit area from marine-terminating (384 ± 16 kg m^{-2} a^{-1}) than from land-terminating basins (209 ± 10 kg m^{-2} a^{-1}). Although an Arctic-wide partitioning between SMB and D is not available before 2010, the disparity between losses from land- and marine-terminating GIC has almost certainly increased compared to the 2000s, given the acceleration of tidewater glaciers in recent years (Strozzi et al., 2017b), and the rapid deflation of a small number of marine-terminating basins (Dunse et al., 2015; Haga et al., 2020; McMillan et al., 2014; Nuth et al., 2019; Strozzi et al., 2017a; Willis et al., 2018). Austfonna Ice Cap alone lost 4.6 ± 0.3 Gt a^{-1} during 2010-2017, a budget dominated by the dynamic activation of Basin 3 since 2012 (McMillan et al., 2014)

(Appendix B). In Severnaya Zemlya, where SMB represents only 6 % of total mass loss, ice dynamics were almost entirely responsible for the negative regional losses between 2010 and 2017 (Table 2), with dynamic thinning dominating mass balance fluctuations in this region since the 1990s (Moholdt et al., 2012a). Elsewhere in the BKS sector, ice discharge accounted for 72 %, 47 % and 13 % of the total mass loss for Franz Josef Land, Svalbard and Novaya Zemlya respectively (Table 2). By unit area, Franz Josef Land, Svalbard and Severnaya Zemlya exhibit the largest rates of dynamic loss D with 212± 49 kg m^{-2} a^{-1}, 188 ± 30 kg m^{-2} a^{-1} and 98 ± 11 kg m^{-2} a^{-1}, respectively (Table 2, Fig. 3). Some of Novaya Zemlya's Barents Sea coast outlet glaciers accelerated during the study period (Carr et al., 2017; Melkonian et al., 2016), contributing to a dynamic imbalance of -51 ± 29 kg m^{-2} a^{-1}. By unit marine-terminating basin area, which highlights the intensity of dynamic instability, Svalbard lost ice via discharge at 277 ± 41 kg m^{-2} a^{-1} owing primarily to Basin 3, followed by Franz Josef Land at 235 ± 54 kg m^{-2} a^{-1}, Severnaya Zemlya at 205 ± 20 kg m^{-2} a^{-1} and Novaya Zemlya at 82 ± 37 kg m^{-2} a^{-1} (Table 2).

Table 2
Summary table of D: the dynamic mass budget is calculated with a constant density of ice equal to 850 kg m^{-3}. Area-specific D is computed relative to the total marine-terminating basin area (*) and relative to the total glaciated area (**) of each region. The last column refers to D as a percentage of total mass balance ($\dot{m}$).

Region	D [Gt a^{-1}]	D_{spec} [kg m^{-2} a^{-1}]*	D_{spec} [kg m^{-2} a^{-1}]**	D / $\dot{m}$
FJL	-2.7 ± 0.6	-235 ± 54	-212 ± 49	72 %
NZ	-1.1 ± 0.5	-82 ± 37	-51 ± 29	13 %
SZ	-1.6 ± 0.2	-205 ± 20	-98 ± 11	94 %
Sv	-6.2 ± 0.9	-277 ± 41	-188 ± 30	47 %
Ic	-	-	-	-
CAA-N	+0.3 ± 1.4	+7 ± 28	+3 ± 23	1 %
CAA-S	+0.3 ± 0.4	+93 ± 137	+7 ± 63	1 %
RAA	-5.4 ± 0.8	-164 ± 25	-108 ± 18	38 %
BKS	-11.6 ± 1.2	-210 ± 22	-138 ± 16	43 %
Total Arctic	-11.0 ± 1.9	-102 ± 17	-46 ± 16	13 %

5. Atmospheric and oceanic drivers of ice loss

Although atmospheric warming is the primary cause of ice loss from the surface of Arctic GIC through increased melting (e.g. Gardner et al., 2011), a broad range of factors affect their discharge. Tidewater glacier dynamics are determined by changing boundary conditions such as shifts in the stress balance at the glacier front, as these can trigger instabilities that can propagate inland rapidly (Dunse et al., 2015; McMillan et al., 2014; Nuth et al., 2019; Willis et al., 2018). The influx of Atlantic Ocean waters and recirculation of warm bottom water in Arctic fjords, the rapid drainage of surface meltwater to the base of glaciers, and submarine melting driven by the buoyant advection of subglacial discharge at calving fronts, are all known to affect rates of tidewater glacier flow (Cook et al., 2019; Cowton et al., 2018; Slater et al., 2016). Decreased sea ice concentrations have also been suggested to impact calving rates and promote the acceleration of ice discharge (Robel, 2017). To investigate the drivers of the recent Arctic GIC dynamic imbalance, we analyse trends in regional atmospheric (Dee et al., 2011) and oceanic (Xie et al., 2017) temperatures, and in sea ice concentrations (Comiso, 2017) (Appendix A11).

The Arctic climate has warmed significantly, and mean surface air temperatures were 0.4 to 2.3 °C higher during our survey period than in the preceding decade (Table 3). However, longer term trends show that, while atmospheric warming has occurred across the region as a whole (Fig. 4), ocean warming and sea ice retreat have been largely restricted to the eastern Arctic, where recent ice stream formation (Zheng et al., 2019) and acceleration of ice flow (Strozzi et al., 2017b) suggest that GIC have experienced significantly increased glacier discharge. For example, across the BKS sector, including Svalbard, Novaya Zemlya, Franz Josef Land, and Severnaya Zemlya, the average rise in sea surface, subsurface, and atmospheric temperatures adjacent to GIC have been 0.6 °C, 0.4°C, and 2.0 °C, respectively, and the average reduction in sea ice concentration has been 9.4 % (Table 3). By comparison, the ocean temperature and sea ice concentration around the Canadian Arctic Archipelagos have changed little**.**

Table 3
Anomalies in air surface temperature (T_{2m}), sea surface temperature (SST), subsurface ocean temperature (SOT), and sea ice concentration (SIC) during the survey period (2010-2017) relative to the previous decade (2000-2009). T_{2m} and SST are from ERA-Interim; SOT is 200m depth ocean temperature from TOPAZ; SIC data are from NASA Team/ bootstrap sea ice algorithm (Appendix A11).

Region	T_{2m} [°C]	SST [°C]	SOT [°C]	SIC [%]
FJL	+2.3	+0.3	+0.3	-13.2
NZ	+2.1	+0.9	+0.6	-8.2
SZ	+1.9	+0.2	+0.3	-7.6
Sv	+1.5	+1.1	+0.5	-8.4
Ic	+0.8	-0.1	+0.2	-0.1
CAA-N	+0.4	+0.1	-0.3	-0.4
CAA-S	+1.3	+0.2	-0.3	-0.5
CAA	+0.9	+0.2	-0.3	-0.5
RAA	+2.1	+0.5	+0.4	-9.7
BKS	+2.0	+0.6	+0.4	-9.4

231
232

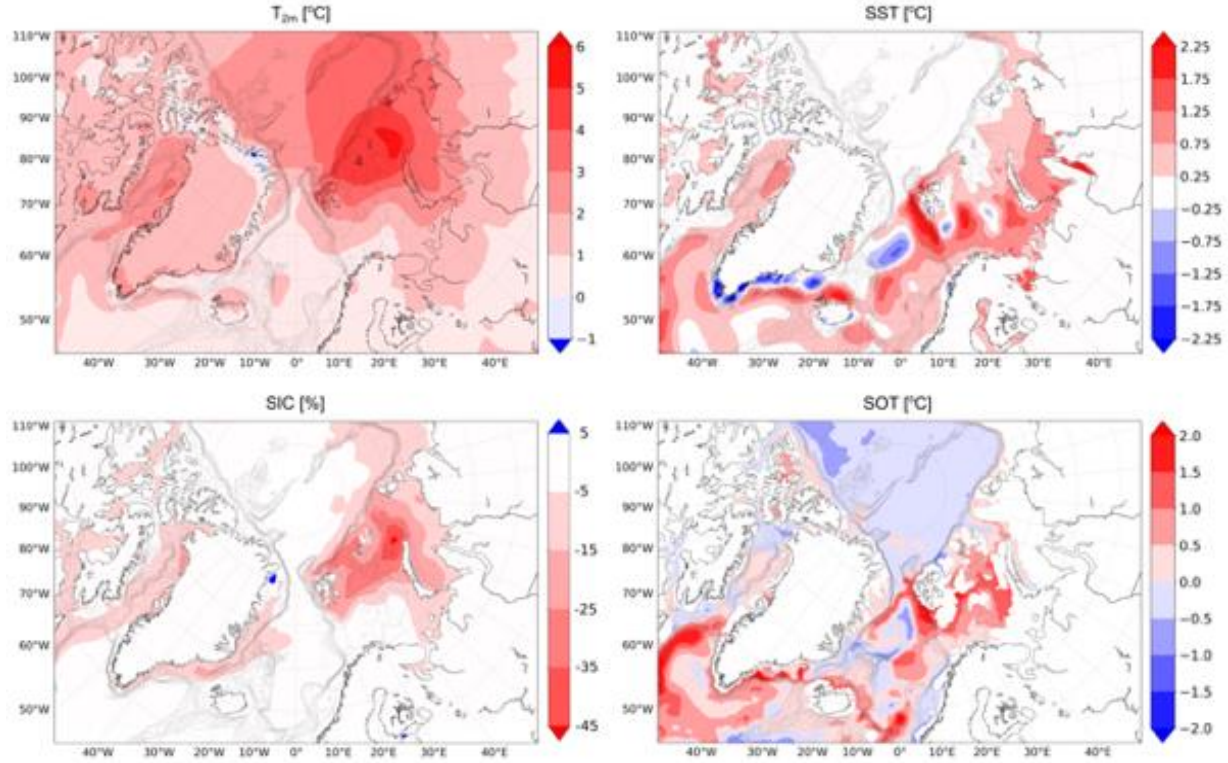

Fig. 4. Arctic climate forcing anomalies. Air surface temperature (T_{2m}), sea surface temperature (SST), subsurface ocean temperature (SOT), and sea ice concentration (SIC) anomalies during the CryoSat-2 period (2010-2017) with reference to the baseline period (1990-1999). Anomalies with reference to the previous decade (2000-2009) are provided in Appendix D.

The warming of the BKS sector has been associated with the combined effects of enhanced storm activity and increased Atlantic Water inflow to the Eurasian and Siberian Shelf seas (Barton et al., 2018; Lind et al., 2018; Polyakov et al., 2017). Farther afield, it has also been shown that the Arctic- and North Atlantic Oscillations are correlated with glacier mass balance (Bjørk et al., 2018; Carr et al., 2017; Ding et al., 2014; Gardner and Sharp, 2006; Moholdt et al., 2012b; Wouters et al., 2019; Zeeberg and Forman, 2001), with opposite effects in the eastern and western Hemispheres depending on the position and strength of the Arctic Circumpolar Vortex (Bjørk et al., 2018; Gardner and Sharp, 2006; Wouters et al., 2019). These modes of large-scale atmospheric variability in the North Atlantic are likely to impact not only SMB via surface warming but also trigger dynamic instabilities by affecting sea ice concentrations and ocean warming in addition to the atmospheric changes, albeit with possible delayed response times and associated regional heterogeneity (Wouters et al., 2019).

6. Conclusions

Using CryoSat-2 swath radar altimetry, we have computed elevation and mass trends for all Arctic GIC outside Greenland with unprecedented (500 m) spatial resolution. Between 2010 and 2017, we estimate they have lost 87.0 ± 2.6 Gt a^{-1} of snow and ice on average, a 7 % increase relative to the 2003-2009 annual mean (Gardner et al., 2013) but with significant regional differences. By modelling the contribution due to SMB, we isolate the elevation change signal due to anomalous glacier flow. Using this approach, we find that SMB is responsible for the vast majority (87 %) of the observed mass loss, while ice discharge has caused the remainder (13 %). However, based on a significant number of independent observations, ice discharge from GIC in the Barents and Kara Sea area has increased since the 2003-2009 period, and now accounts for 43 % of the mass loss from this region. This enhanced dynamic signal has been occurring in conjunction with increased air and ocean temperatures, and loss of sea ice (e.g. Morris et al., 2020).

It is predicted that, even when excluding tidewater glacier discharge, losses from the Canadian Arctic Archipelagos and the BKS will be dominating glacier and ice cap mass losses outside the Greenland and Antarctic Ice Sheets in future climate scenarios (Möller et al., 2016; Radić et al., 2014). Most importantly, while SMB is projected to be the prevalent mechanism of Greenland ice loss in the coming decades (Enderlin et al., 2014; Nick et al., 2013; Price et al., 2011), a recent study finds that D, not SMB has dominated ice losses in Greenland over the past half-century (Mouginot et al., 2019). Our results show that the dynamic response of marine-terminating GIC to climate forcing makes up a significant proportion of the total mass budget in the rest of the Arctic since 2010, with D contributing up to ten times the losses from SMB in some regions, and with rapid and significant temporal fluctuations. This pattern is likely to endure over time, as the large number of Arctic tidewater glaciers will continue to respond to receding sea ice and to the impinging Atlantification of Arctic Ocean basins. We also emphasise the need for caution when extrapolating in space and time observations of glacier changes from a limited number of basins, and encourage the development and use of high-resolution, large-scale observations of surface elevation, SMB, ice thickness and velocity to improve the quantitative assessment of ice discharge. This is an essential step towards a more accurate representation of dynamic imbalance in the parametrisation of climate models, and towards reducing uncertainty in the projections of future ice mass loss in a changing climate.

Acknowledgments

This work was performed under the European Space Agency (ESA) Support to Science Elements CryoSat+ CryoTop contract 4000107394/12/I-NB, CS+ Mountain Glaciers contract 4000114224/15/I-SBo to N.G. The authors would like to thank ESA for providing open access to CryoSat-2 data, NASA for providing access to Operation Ice Bridge, and Dr. B.P.Y. Noël for access to RACMO2.3 data.

Appendix A. Methods

A1. Elevation data. We use surface elevation data between 07/2010 and 07/2017 from the SAR Interferometric Radar Altimeter (SIRAL) onboard the European Space Agency (ESA) CryoSat-2 satellite (Wingham et al., 2006). SIRAL is a beam-forming active microwave radar altimeter with a maximum imaging range of ~15 km on the ground. The sensor emits time-limited *Ku-band* pulses aimed at reducing the footprint to ~1.6 km within the beam. Over Arctic GIC, the sensor operates in synthetic aperture interferometric (SARIn) mode, which allows delay-Doppler processing to increase the along-track resolution to ~380 m, while cross-track interferometry is used to extract key information about the position of the footprint center (Gray et al., 2015). CryoSat-2 orbits the Earth with a 369-day repeat period formed by the successive shift of a 30-day sub-cycle. The satellite has an inclination of 92°, offering complete coverage of the Arctic GIC and a rapid increase in orbit cross-over density towards the poles - from 7.5 km inter-track distance at the Equator to less than 1.6 km at latitudes higher than 70° (Gourmelen et al., 2018; Wingham et al., 2006).

A2. Swath processing. We process *level 1b,* baseline C data supplied by the ESA ground segment using a swath processing algorithm. *Level 1b* data is provided as a sequence of radar echoes along the satellite track, which translates into single power, interferometric phase and coherence waveforms for each along-track sampling location (Gourmelen et al., 2018). The conventional *level 1b* data processing method consists of extracting single elevation measurements from the power signal in each waveform that corresponds to the Point of Closest Approach (POCA) between satellite and the ground. In contrast, swath altimetry exploits the full radar waveform to map a dense swath (~5 km wide) of elevation measurements across the satellite ground track beyond POCA (Christie et al., 2016; Foresta et al., 2016; Gourmelen et al., 2018; Gray et al., 2013; Ignéczi et al., 2016). Swath processing provides one to two orders of

magnitude more elevation measurements compared with POCA (Foresta et al., 2016; Gourmelen et al., 2018) and alternative satellite instruments (Appendix E).

A3. Gridded topography and elevation change. Gridded elevation is computed using a plane-fit algorithm for the entire measurement period, 2010-2017. The dense elevation field *h(x, y, t)* allows gridding with a cell resolution of 500 by 500 m to ensure sufficient spatial detail while maximising the number of observations in each resolution cell (Foresta et al., 2016). The measurements sampled within 500 m from each pixel center (x_p,y_p) are expressed as a function of easting *(x)*, northing *(y)*, and time *(t)*:

$$h(x, y, t) = c_0\, x + c_1\, y + c_2\, t + c_3 = \nabla h(x, y) + \dot{h} t + c$$

with

$$\nabla h(x, y) = \frac{\partial h}{\partial x} x + \frac{\partial h}{\partial y} y \qquad \text{and} \qquad \dot{h} = \frac{\partial h}{\partial t}$$

$\nabla h(x, y)$ is the ice surface gradient, and the time-dependent coefficient c_2 retrieved from the linear fit is the rate of surface elevation change $\dot{h}$. The gridded elevations $h_p(x_p,y_p)$ are fitted to the measurement field around each pixel center using an iterative 3σ-filter at each step until all outliers are removed (Foresta et al., 2016).

A4. Validation. We compare CryoSat-2 gridded $\dot{h}$ at 500 m posting with airborne records from the NASA Operation Ice Bridge (OIB) Airborne Topographic Mapper (ATM). We were able to locate two single validation test sites in the Arctic beyond Greenland with measurements sampled after the launch of CryoSat-2: Barnes Ice Cap on Baffin Island, and Devon Ice Cap on Devon Island, Canadian High Arctic. The data drawn for comparison is NASA IceBridge ATM L4 Surface Elevation Rate of Change, Version1 (Studinger, 2014), sampled along extensive OIB repeat flight paths in 2010 and 2015. We match these data with $\dot{h}$ generated from CryoSat-2 measurements acquired between 2010 and 2015. The validation is constrained to OIB measurements that are within 250 m of the CryoSat-2 $\dot{h}$ grid centre (1/2 grid spacing). We calculate a measurement bias

as the median value of the difference between swath products and OIB measurements (that is, CryoSat-2 swath minus OIB). Validation of rates of $\dot{h}$ yields a minimal bias of 0.05 m a^{-1} $\pm$ 0.26 m a^{-1} and 0.00 m a^{-1} $\pm$ 0.13 m a^{-1} respectively for Barnes and Devon Ice Caps (Appendix F). The small difference can arise from differences in spatial and temporal resolution and/or signal properties. We also inspected elevation time-series to ensure that rates of change were not affected by spurious elevation biases related to changes in the scattering horizon (McMillan et al., 2014; Nilsson et al., 2016). A more complete validation exercise of CryoSat-2 swath products was performed by Gourmelen et al. (2018) over parts of the Greenland- and Antarctic Ice Sheets.

A5. Ice masks. We use ice masks to delimit the regions covered in ice from bare ground and ocean water in all gridded products. The masks are also used to differentiate between pixels pertaining to land- *versus* marine-terminating basins. They are retrieved in vector (*shp*) format from the Randolph Glacier Inventory (RGI) 6.0, available at Global Land Ice Measurements from Space (GLIMS). Partitioning between land- and marine-terminating basins needed to be corrected for misallocations in RGI 6.0 for some regions. Most substantial adjustments were made for Svalbard, where a number of land-terminating basins needed to be re-allocated as marine-terminating based on visual inspection of online maps from the Norwegian Polar Institute available at www.npolar.no. Reallocation was made for the following GIC basins/ glaciers: Augnebreen, Aldousbreen, Besselsbreen, Bragebreen, Deltabreen, Duckwitzbreen, Fjortende Julibreen, Franklinbreen N and S, Frazerbreen, Gimlebreen, Hayesbreen, Hochstetterbreen, Idunbreen, Infantfonna, Ingerbreen, Innifonna, Johansenbreen, Kongsbreen, Kongsvegen, Kronebreen, Mittag-Lefflerbreen, Monacobreen, Negribreen, Nordenskiöldbreen, Nordsysselbreen, Oslobreen, Paulabreen, Petermannbreen, Polarisbreen, Recherchebreen, Scheibreen, Sidevegen, Spælbreen, Stonebreen, Tunabreen, Vaigattbreen.

The following Arctic sub-regions are covered by GIC but were not included in this study as CryoSat-2 does not operate in SARIn mode at their location (see CryoSat-2 Geographical

Mode Mask, https://earth.esa.int/web/guest/-/geographical-mode-mask-7107, accessed on 02/04/2019): Jan Mayen, Kvitøya Ice Cap (Sv), Victoria Ice Cap (FJL), Ushakov Ice Cap (Ushakov Island, RAA), Schmidt Ice Cap (SZ). Together these ice masses extend over a relatively small glaciated area (~1600 km^2). The De Long Islands ice caps (East-Siberian Sea, RAA) were also excluded due to their small size (total glaciated area < 80 km^2 (Glazovskiy, 1996).

For all regions, we assume that during the period of measurement, the glaciated area remains constant. Information on imagery acquisition date, type of processing and source/ authorship is described in the GLIMS Technical Report 'Randolph Glacier Inventory – A Dataset of Global Glacier Outlines: Version 6.0' (https://www.glims.org/RGI/00_rgi60_TechnicalNote.pdf, accessed on 27/11/2020). For each of the regions defined in our study, this information is summarised below:

CAAN	1999-2003 2000-2003	Landsat 7 (ETM+) ASTER
CAAS	 1958/1982 2006-2010 1999-2002	Compiled from CanVec maps (Natural Ressources Canada) Aerial photographs SPOT5 Landsat 7 (ETM+)
Iceland	1999-2004	ASTER and SPOT5
Svalbard		Variety of sources and additions. Mainly SPOT5-HRS DEMs and orthoimages
RAA	2000-2010	Manually digitised from SPIRIT SPOT5 and Landsat imagery

A6. Volume change. We use surface elevation changes from our gridded $\dot{h}$ maps to calculate volume change rates $\dot{V}$ over the entire Arctic between 2010 and 2017. Volumetric changes are

computed as the sum of the gridded surface elevation change rates from each pixel of a denoised gridded $\dot{h}$ product multiplied by the pixel area as defined by the posting (0.5 km^2 per pixel):

$$\dot{V}_{denoised} = A_{pixel} \cdot \sum \dot{h}_{denoised}$$

Denoising is performed for each region separately by removing pixels with values of $|\dot{h}| >$ δ, and errors (variances) $\varepsilon_{\dot{h}}$ on $\dot{h}$ above a certain threshold. We choose δ = 25 m a^{-1} and δ = 50 m a^{-1} for land- and marine-terminating basins, respectively, as the maximum realistic rates of change. Errors $\varepsilon_{\dot{h}}$ are extracted from the covariance matrix of the plain-fit algorithm used to compute gridded elevations (Foresta et al., 2016). We select an appropriate error threshold by iteratively computing $\dot{V}_{denoised}$ while increasing the allowed maximum error $\varepsilon_{\dot{h}}$ at each step until $\dot{V}_{denoised}$ converges towards a plateau value. The final error threshold $\varepsilon_{\dot{h},\,\boldsymbol{thres}}$ is chosen so that the number of outliers is minimised after $\dot{V}_{denoised}$ converges. Error thresholds vary between 3 ± 2 m a^{-1} and are specific for each region.

To calculate the total volume change $\dot{V}$, we make assumptions about areas not covered by measurements or where outliers were removed. For the land-terminating segments we assume that SMB processes largely dominate the overall mass budget, and we fill the data gaps by applying hypsometric averaging following the method used in Foresta et al. (2016) (Appendix B). This approach is not applicable for marine-terminating basins however, where dynamic processes often lead to significant geometric changes over the ice surface, and hence, a simple relationship between $\dot{h}$ and elevation is not sufficient to describe volume loss. Thanks to the high density of observations provided by CryoSat-2 (Appendix B), particularly for the marine-terminating sectors of Franz Josef Land, Novaya Zemlya, Severnaya Zemlya, and Svalbard, we rescale $\dot{V}_{denoised}$ using the ratio of total-to-measured glaciated area:

$$\dot{V} = \frac{n_{total}}{n_{denoised}} \cdot \dot{V}_{denoised}$$

where n_{total} is the total number of pixels and $n_{denoised}$ the number of pixels in the denoised $\dot{h}$ product. Upscaling was applied over the total marine-terminating basin area of the seven regions in Table 1. We performed a sensitivity test of the upscaling method by comparing against hypsometric averaging over the land-terminating area of single CAA ice caps (Appendix B). Both CAA-N and CAA-S are characterised by rugged topography and are the regions with lowest data coverage. The comparison reveals little difference in the mass budget between the two regionalisation schemes. We therefore apply upscaling as a method to fill data gaps in the marine-terminating segments of all Arctic GIC, including CAA-S and CAA-N.

A7. Mass change. The conversion from volume to mass change is performed using a constant density of ice ρ_{ice} equal to 850 $\pm$ 60 kg m^{-3} as advocated by (Huss, 2013) to better account for a wide range of surface conditions. For each of the seven regions in Table 1 we apply the appropriate regionalisation scheme to the sum of all land- and marine-terminating basins separately, and compute the corresponding land- and marine-terminating mass budgets ($\dot{m}_{l}$ and $\dot{m}_{m}$, respectively) (Appendix B). The total mass balance $\dot{m}$ is then calculated as the sum of the two segments:

$$\dot{m} = \dot{m}_{l} + \dot{m}_{m}$$

Computing mass budgets on a single ice cap basis brings insignificant changes to the overall result (Appendix B), with differences well within error margins. For the CAA, this confirms similar findings by Gardner et al. (2011). Specific mass balance is calculated as the ratio of mass change to surface area, whereby the glaciated area extent is based on the glacier outlines from RGI 6.0.

A8. Partitioning total mass balance into SMB and D. Local elevation changes over the ice surface occur as a result of surface mass balance (SMB) anomalies and the advection of ice masses (D) and are described by the kinematic relation for $\dot{h}$ (*e.g.* Cuffey and Paterson, 2010).

To quantify the relative contribution of SMB and D to the overall mass loss, we parametrise elevation change ($\dot{h}_l$) as a function of elevation (h_l) and spatial coordinates (x_l, y_l) over the sum of all land-terminating GIC basins only, for each of the seven regions listed in Table 1:

$$\dot{h_l} \approx a_0\, {h_l}^3 + a_1\, {h_l}^2 + a_2\, h_l + a_3\, x_l + a_4\, y_l + a_5$$

The function describes the direct influence of elevation, latitude and longitude on SMB-related elevation change $\dot{h}_l$. The order of fit was derived from the convergence of R^2 statistics of a series of polynomial functions that best describe the regional sample distributions, an approach developed previously for hypsometric averaging of surface elevation change (Foresta et al., 2016; Moholdt et al., 2010; Nilsson et al., 2015; Nuth et al., 2010). The applied method is a trade-off between capturing the regional x, y, h trends while ensuring stability of the parametrisation. We use the coefficients a_i (Appendix G) of the fit and gridded elevations $h_l\,(x_l, y_l,$ t*)* and $h_m\,(x_m, y_m,$ t*)* over land- and marine-terminating sectors, respectively, to calculate parametrised $\dot{h}_{p_l}$ and $\dot{h}_{p_m}$, separately for both types of basins. We derive bulk marine-terminating SMB_m as follows:

$$SMB_m = SMB_l \cdot \sum_{n_m} \dot{h}_{p_m} \;/\; \sum_{n_l} \dot{h}_{p_l}$$

where SMB_l is equal to the total mass balance $\dot{m}_{\,l}$ of the sum of all land-terminating GIC basins in each region (Appendix A7), and n_l and n_m are the number of pixels in the gridded $\dot{h}_{p_l}$ and $\dot{h}_{p_m}$ maps, respectively. We then calculate D by subtracting SMB_m from the total mass balance $\dot{m}_{\,m}$ of marine-terminating GIC basins. To evaluate our parametrisation of $\dot{h}_l$ we calculate the root mean square error (RMSE) of the polynomial fit as:

$$RMSE = \sqrt{\frac{\sum\left(\dot{h}_{p_l} - \dot{h_l}\right)^2}{\mathrm{n}}}$$

where n is the number of grid cells. RMSE values vary regionally and range between 0.53 m a^{-1} and 6.41 m a^{-1}.

A9. SMB comparison CryoSat-2 - RACMO2.3. To evaluate our method for partitioning mass imbalance into SMB and D, we use seven glaciological years (10/2010 - 09/2017) of monthly area-specific SMB data for CAA-N and CAA-S from the Regional Climate Model RACMO2.3. The dataset and the corresponding ice masks are down-sampled to 1 km (Noël et al., 2018). We produce additional ice masks at 1 km resolution for marine- and land-terminating basins separately for both CAA-N and CAA-S based on the RGI 6.0 split between the two types of basins. Annual SMB is calculated pixelwise for each year and then integrated over the entire area to obtain total SMB by region and terminus type. SMB derived from CryoSat-2 swaths are in excellent agreement with SMB from RACMO2.3 across both CAA's land- and marine-terminating basins (Figure 2a,b).

In the eastern Arctic, Svalbard's 2010-2017 dynamic imbalance D (-6.2 ± 0.9 Gt a^{-1}) (Table 2**)** is in good agreement with calving rates from Blaszczyk et al. (2009) (-6.1 ± 1.5 Gt a^{-1}), which to date is the only available study to have quantified the frontal ablation of Svalbard's glaciers and ice caps (Schuler et al., 2020). Nevertheless, a number of independent observations suggest a likely increase in dynamic ice loss from Svalbard's tidewater glaciers during the 2010s with respect to the previous decade (McMillan et al., 2014; Nuth et al., 2019; Strozzi et al., 2017a), which would imply that either Blaszczyk et al.'s estimate based on 2000-2006 composite snapshots was overestimated, or bulk D derived from the CryoSat-2 data parametrisation is underestimated.

A10. Errors. The uncertainty associated with the calculated mass imbalance is the result of unknown density fluctuations, gradients in snow accumulation, and errors in elevation trends from the satellite measurements. The elevation measurement errors can be attributed to instrument system errors (intrinsic to *level 1b* data) on one hand, and to sampling errors in the swath processing algorithm on the other hand. We estimate a representative uncertainty of the mass imbalance, using the same method as in Foresta et al. (2016). We account for errors in the

measurement statistically by extracting from the covariance matrix of our surface elevation fit the variances $\varepsilon_{\dot{h}}$ that are assigned to the rates of $\dot{h}$ (Foresta et al., 2016). Depending on the type of drainage basin, the error on volume change $\varepsilon_{\dot{V}}$ is obtained by propagating $\varepsilon_{\dot{h}}$ either by hypsometric averaging (land-terminating basins), or rescaling by the ratio of total-to-measured surface area (marine-terminating basins). For the volume-to-mass conversion we assume a constant error on the density ε_{ρ} = 60 kg m^{-3} following Huss (2013). The error on the mass imbalance is calculated using uncorrelated Gaussian error propagation as:

$$\varepsilon_{\dot{m}} = |\dot{m}| \cdot \sqrt{\left(\frac{\varepsilon_{\dot{V}}}{\dot{V}}\right)^2 + \left(\frac{\varepsilon_{\rho}}{\rho_{ice}}\right)^2}$$

For land-terminating drainage basins we assume that $\varepsilon_{\dot{m}} = \varepsilon_{SMB}$. SMB uncertainties of marine-terminating basins are estimated by assigning the root mean square deviation of our SMB parametrisation to the error $\varepsilon_{\dot{h}}$ on $\dot{h}$, and applying Gaussian error propagation as described above. For D we derive uncertainties ε_D from the quadrature of $\varepsilon_{\dot{m}}$ and ε_{SMB}:

$$\varepsilon_D = \sqrt{(\varepsilon_{\dot{m}})^2 + (\varepsilon_{SMB})^2}$$

Satellite coverage is typically > 98 % and > 80 % of the total glaciated area in the BKS and the CAA, respectively (Appendices C1-C6). The measured areas after the removal of noise (or spurious data) are given for each GIC region in Appendix B. The spurious estimates of elevation change are randomly distributed across the glaciated area although in a few locations under-sampling occurs at low elevations, where stronger thinning generally prevails. This could lead to a local underestimation of the losses, in particular from marine-terminating GIC segments, where upscaling of volume change is applied (Appendix A6). This is not accounted for as a source of uncertainty in this study. However, given the very low number of spurious samples compared to the total number of measurements, especially in the archipelagos of the eastern Arctic (Appendices A6, B and C1-C4), this underestimation should be very small. In the case of the CAA, the coverage is generally lower than in the BKS region. Nevertheless, the elevation changes

498 across the CAA display much more homogeneous patterns of change across both land- and
499 marine-terminating catchments compared to the BKS (Appendices C1-C6), which helps keep the
500 errors low on the upscaling method. Hence, overall, the large proportion of valid measurements
501 across the Arctic (Appendix B), and their homogenous distribution over the ice mass surfaces
502 (Appendices C1-C6) is sufficient to be representative of the overall mass balance of marine-
503 terminating GIC basins, thereby justifying the applicability of the upscaling method used.

504 Ice masks are based largely on satellite imagery from the 2000s, although data sources
505 and time of acquisition used for glacier delineation vary by region (Appendix A5). The time lag
506 between glacier outline delineation and CryoSat-2 measurements thus forms a potential source
507 of error in our nominal mass balance estimates, in particular in locations where frontal advance
508 and retreat of glacier termini have been significant over the past two decades, such as in certain
509 catchments Svalbard and in the Russian Arctic. However, we assume that glacier advance and
510 retreat are small compared to the total glaciated area of Arctic GIC, and hence we imply that the
511 related uncertainty remains insignificant at the Arctic scale. For example, regions characterised
512 by surge-type glacier behaviour with rapid deflation of the ice masses, resulting in a redistribution
513 of the ice masses beyond the applied glacier delimitations, are limited to a small number of basins.
514 Although some level of uncertainty associated with changes in glacier delineation remains, it is
515 beyond the scope of this paper to account for them quantitatively for each region. However, in
516 order to provide a rough idea of what these may represent at the Arctic scale, we refer to McMillan
517 et al. (2014) who estimated a net terminus advance of 50 km^2 at Austfonna's Basin 3 from 2010
518 to 2014. This is one of the most dramatic advances experienced by an Arctic ice cap during the
519 CryoSat-2 era, representing ~0.64 % of the Austfonna ice cap area (7800 km^2), and ~0.15 % of
520 Svalbard's glaciated area (33200 km^2). Nonetheless, we expect that uncertainties related to
521 changes in glacier area due to an increase in land-terminating glacier surges, and to terminus
522 retreat inside the defined glacier outlines, may impact estimates of sea-level contribution
523 increasingly in the future in the absence of regular updates of the RGI glacier inventories.

A11. Climate forcing. We use maps of monthly mean SST and T_{2m} on a 0.75° x 0.75° grid from ECMWF Interim Reanalysis (ERA-I) (Dee et al., 2011), with the smallest bias from observations (Lindsay et al., 2014). We extract 200 m depth SOT from the Arctic Ocean reanalysis TOPAZ (Xie et al., 2017) on a 12-16 km grid, and analysed for the 15th day of each month. The passive microwave NASA Team (Cavalieri et al., 2019) and Bootstrap (Comiso, 2017) SIC data are monthly means on a 25 km by 25 km polar stereographic grid. Regional averages surrounding each GIC (values in Table 3) are calculated by nearest neighbour interpolation from the native grids of each forcing over the target regions (as defined by the rasterised RGI 6.0 glacier outlines) in Fig. 1.

A12. Data availability. Our swath processing algorithm uses SARIn-mode CryoSat-2 *Level 1b* format data directly downloaded from ftp://science-pds.cryosat.esa.int (accessed on 27/06/2019); NASA Operation Ice Bridge validation data is available for download at https://nsidc.org/data/icebridge (accessed on 27/06/2019); ice masks for all regions except Iceland were taken from https://www.glims.org/RGI/rgi60_dl.html (accessed on 27/06/2019); RACMO data is available for download at https://doi.pangaea.de/10.1594/PANGAEA.881315; the passive microwave NASA Team and Bootstrap concentration data are available respectively from http://nsidc.org/data/nsidc-0051 and http://nsidc.org/data/nsidc-0079; The ARCTIC_REANALYSIS_PHYS_002_003 TOPAZ product is available from http://marine.copernicus.eu/services-portfolio/access-to-products; ERA-Interim monthly means of daily means are available from https://apps.ecmwf.int/datasets/.

Appendix B. Mass balance of Arctic GIC. Split by type of basin (marine- and land-terminating), comparison of upscaling (S) *versus* hypsometric averaging (H) as regionalisation schemes of land-terminating basins. $A_{measured}$ refers to the proportion (as a percentage) of the total GIC area that has reliable observations after the removal of spurious data points.

Region / GIC	Total MB	Marine-terminating basins		Land-terminating basins		
	[Gt a^{-1}]	S [Gt a^{-1}]	$A_{measured}$ / A_{total}	S [Gt a^{-1}]	H [Gt a^{-1}]	$A_{measured}$ / A_{total}
FJL	**-3.8 ± 0.3**	**-3.7 ± 0.3**	**90%**	**-0.2 ± 0.0**	**-0.1 ± 0.0**	**88%**
Windy	+0.3 ± 0.0	+0.2 ± 0.0	86%	+0.1 ± 0.0	+0.1 ± 0.0	82%
NZ	**-8.5 ± 0.4**	**-5.2 ± 0.4**	**83%**	**-3.0 ± 0.2**	**-3.3 ± 0.2**	**70%**
SZ	**-1.7 ± 0.1**	**-1.6 ± 0.1**	**90%**	**0.1 ± 0.0**	**-0.1 ± 0.0**	**82%**
Sum GIC and upscale	-1.7 ± 0.1	-1.6 ± 0.1		0.1 ± 0.0	-0.1 ± 0.0	
Academy of Sciences	-1.0 ± 0.1	-1.1 ± 0.1	94%	+0.1 ± 0.0	+0.1 ± 0.0	95%
Vavilov	-0.2 ± 0.0	-0.3 ± 0.0	94%	+0.1 ± 0.0	+0.1 ± 0.0	87%
Albanov	0.0 ± 0.0			0.0 ± 0.0	0.0 ± 0.0	83%
Pioneer	0.0 ± 0.0			0.0 ± 0.0	0.0 ± 0.0	82%
Rusanov	-0.2 ± 0.0	-0.1 ± 0.0	87%	-0.1 ± 0.0	-0.1 ± 0.0	76%
Karpinsky	-0.1 ± 0.0	-0.2 ± 0.0	84%	+0.1 ± 0.0	+0.1 ± 0.0	79%
University	+0.1 ± 0.0	0.0 ± 0.0	87%	+0.1 ± 0.0	+0.1 ± 0.0	85%
Semenov-Tyan-Shansky + Kropotkin + Leningradsky	-0.2 ± 0.0	0.0 ± 0.0	75%	-0.2 ± 0.0	-0.2 ± 0.0	76%
Sv	**-13.3 ± 0.8**	**-10.8 ± 0.8**	**85%**	**-2.5 ± 0.2**	**-2.5 ± 0.2**	**69%**
Sum GIC and upscale	-13.8 ± 0.4	-11.2 ± 0.4		-2.6 ± 0.1	-2.6 ± 0.1	
Austfonna	-4.6 ± 0.3	-4.6 ± 0.3	98%	0.0 ± 0.0	0.0 ± 0.0	89%
Vestfonna	-0.4 ± 0.0	-0.4 ± 0.0	95%	0.0 ± 0.0	0.0 ± 0.0	90%
Barentsøya	-0.2 ± 0.0	-0.1 ± 0.0	92%	-0.1 ± 0.0	-0.1 ± 0.0	90%
Edgeøya	-0.9 ± 0.0	-0.5 ± 0.0	90%	-0.4 ± 0.0	-0.4 ± 0.0	84%
NW Spitzbergen	-2.7 ± 0.1	-1.9 ± 0.1	77%	-0.8 ± 0.1	-0.8 ± 0.1	58%
NE Spitzbergen	-0.7 ± 0.0	-0.4 ± 0.0	82%	-0.3 ± 0.0	-0.3 ± 0.0	67%
S Spitzbergen	-4.0 ± 0.2	-3.1 ± 0.2	74%	-0.8 ± 0.1	-0.9 ± 0.1	67%
Ic	**-2.6 ± 0.2**			**-1.2 ± 0.1**	**-2.6 ± 0.2**	**80%**
Sum GIC and upscale	-2.6 ± 0.1			-1.4 ± 0.1	-2.6 ± 0.1	
Vatnajökull	-1.6 ± 0.1			-0.9 ± 0.1	-1.6 ± 0.1	84%
Langjökull	-0.3 ± 0.0			-0.3 ± 0.0	-0.3 ± 0.0	77%
Hofsjökull	-0.2 ± 0.0			-0.1 ± 0.0	-0.2 ± 0.0	84%
Mýrdalsjökull + Eyafjallajökull	-0.1 ± 0.0			+0.1 ± 0.0	-0.1 ± 0.0	63%
Drangajökull	-0.1 ± 0.0			+0.1 ± 0.0	-0.1 ± 0.0	67%
CAA-N	**-32.3 ± 1.6**	**-13.3 ± 0.9**	**63%**	**-17.9 ± 1.3**	**-19.0 ± 1.3**	**62%**
Sum GIC and upscale	-32.6 ± 0.8	-12.9 ± 0.4		-18.0 ± 0.6	-19.7 ± 0.6	
N Ellesmere	-9.4 ± 0.5	-2.7 ± 0.2	56%	-6.0 ± 0.4	-6.7 ± 0.5	57%
Agassiz	-5.0 ± 0.3	-1.5 ± 0.1	52%	-3.1 ± 0.2	-3.5 ± 0.3	64%
Muller	-2.8 ± 0.2	-0.2 ± 0.0	41%	-2.4 ± 0.2	-2.6 ± 0.2	59%
Steacie	-1.8 ± 0.1			-1.6 ± 0.1	-1.8 ± 0.1	50%
Prince of Wales	-5.9 ± 0.3	-4.1 ± 0.3	61%	-1.7 ± 0.1	-1.8 ± 0.1	62%
Sydkap	-0.8 ± 0.0	-0.2 ± 0.0	55%	-0.6 ± 0.0	-0.6 ± 0.0	71%
Manson	-1.7 ± 0.1	-1.4 ± 0.1	71%	-0.3 ± 0.0	-0.3 ± 0.0	53%
Devon	-4.3 ± 0.2	-2.9 ± 0.2	83%	-1.3 ± 0.1	-1.4 ± 0.1	82%
CAA-S	**-24.8 ± 1.8**	**-1.3 ± 0.1**	**37%**	**-23.1 ± 1.6**	**-23.5 ± 1.8**	**56%**
Sum GIC and upscale	-24.5 ± 0.7	-1.5 ± 0.1		-22.7 ± 0.7	-23.0 ± 0.7	
Bylot	-2.3 ± 0.2	-0.2 ± 0.0	67%	-2.2 ± 0.2	-2.1 ± 0.2	54%
Barnes	-4.5 ± 0.3			-4.5 ± 0.3	-4.5 ± 0.3	97%
Penny	-4.3 ± 0.3	-0.8 ± 0.1	11%	-3.5 ± 0.2	-3.5 ± 0.3	44%
N Baffin	-2.3 ± 0.2	-0.2 ± 0.0	39%	-2.0 ± 0.1	-2.1 ± 0.2	51%
Central Baffin	-5.2 ± 0.4	-0.2 ± 0.0	50%	-4.8 ± 0.3	-5.0 ± 0.4	50%
S Baffin	-3.8 ± 0.3			-3.7 ± 0.3	-3.8 ± 0.3	42%
CAA	-57.1 ± 2.4	-14.5 ± 0.9	61%	-41.0 ± 2.1	-42.6 ± 2.2	60%
RAA	-14.0 ± 0.5	-10.5 ± 0.5	87%	-3.1 ± 0.2	-3.5 ± 0.2	77%
BKS	-27.3 ± 0.9	-21.3 ± 0.9	86%	-5.6 ± 0.3	-6.0 ± 0.3	73%
Total Arctic	**-87.0 ± 2.6**	**-35.8 ± 1.3**	**74%**	**-47.8 ± 2.1**	**-51.2 ± 2.3**	**64%**

Appendix C1. Surface elevation change rates (2010-2017) over Svalbard at 500 x 500 m resolution. Spurious elevation changes removed during the post-processing stage are included in the map.

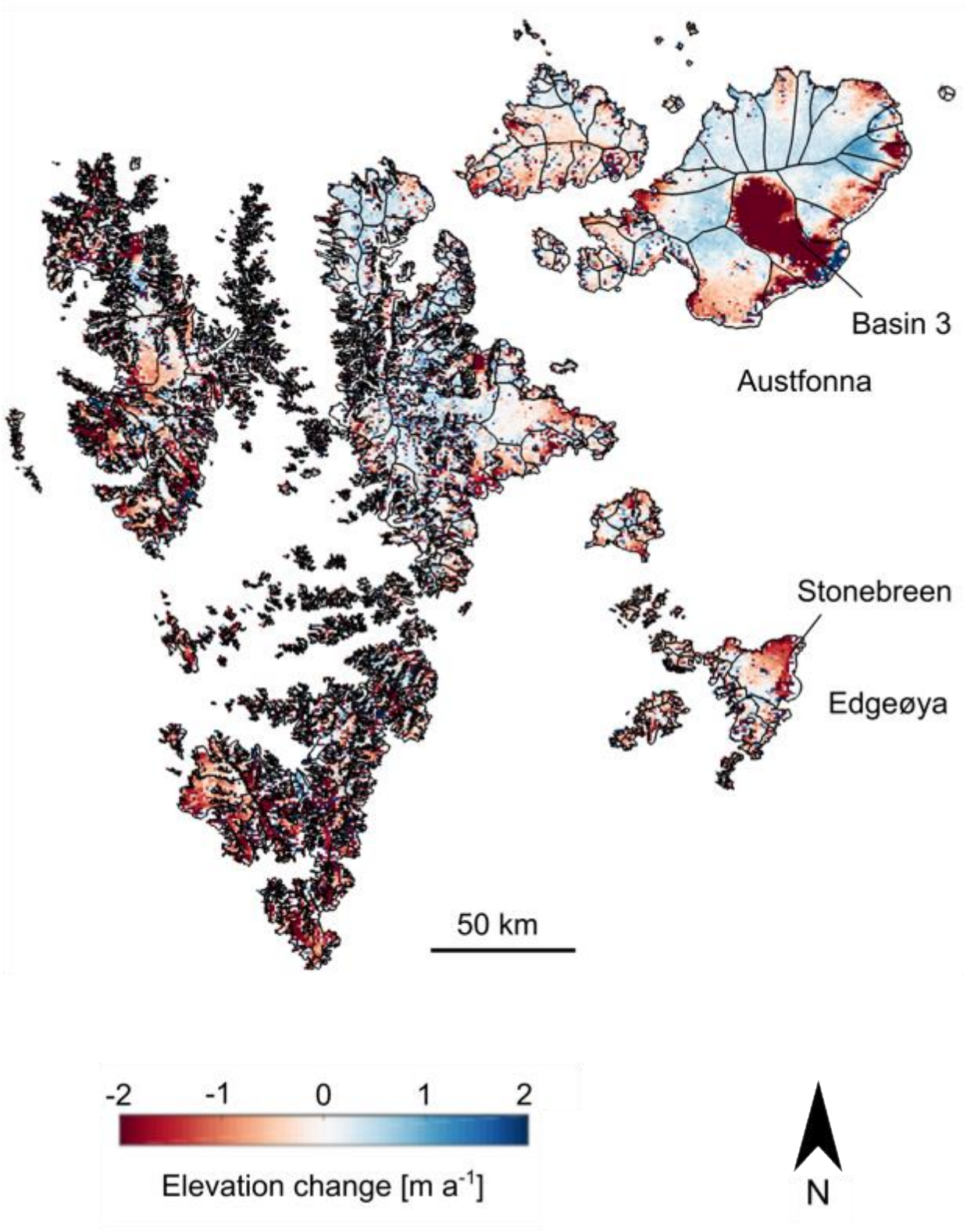

Appendix C2. Surface elevation change rates (2010-2017) over Franz Josef Land at 500 x 500 m resolution. Spurious elevation changes removed during the post-processing stage are included in the map.

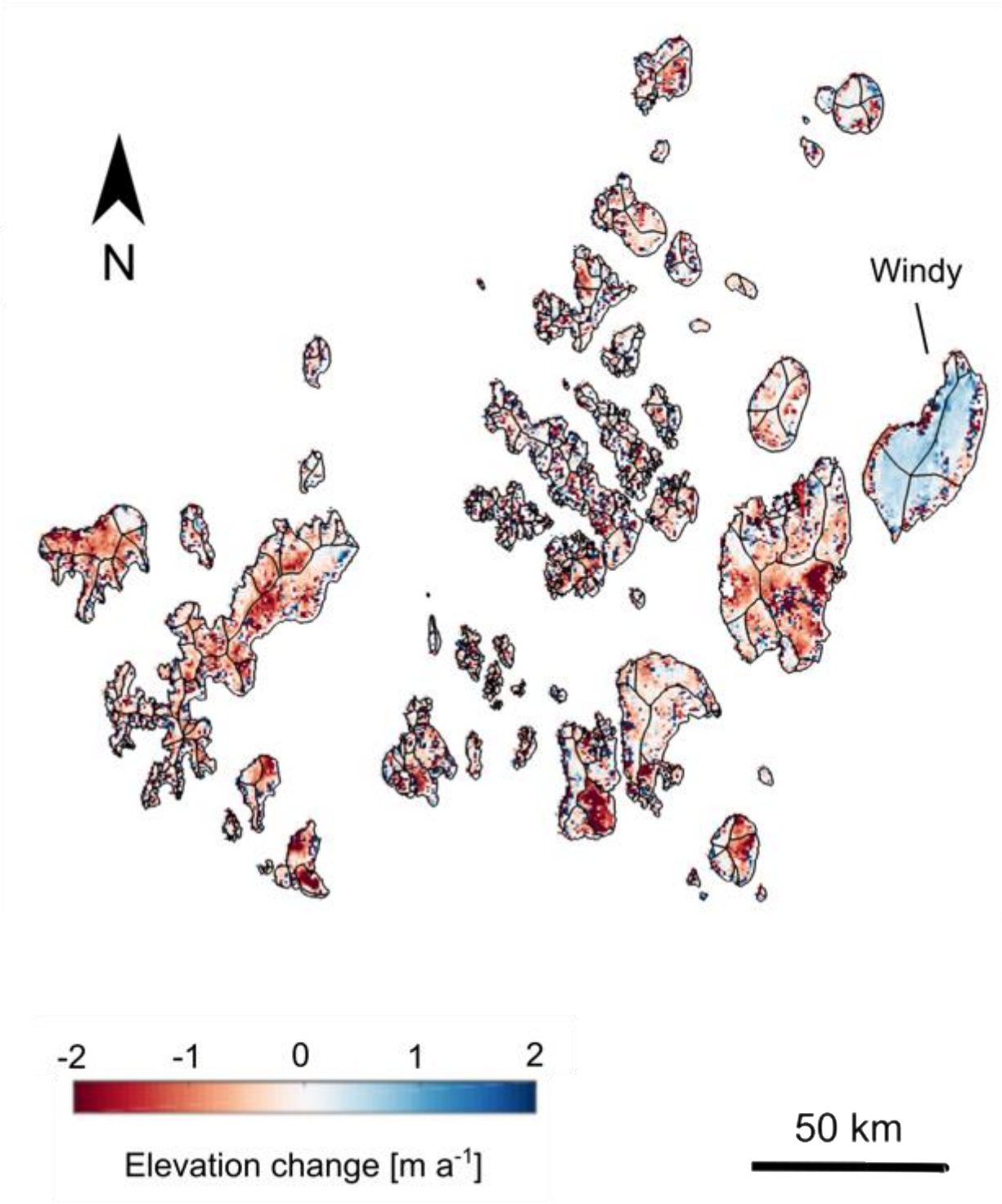

Appendix C3. Surface elevation change rates (2010-2017) over Novaya Zemlya at 500 x 500 m resolution. Spurious elevation changes removed during the post-processing stage are included in the map.

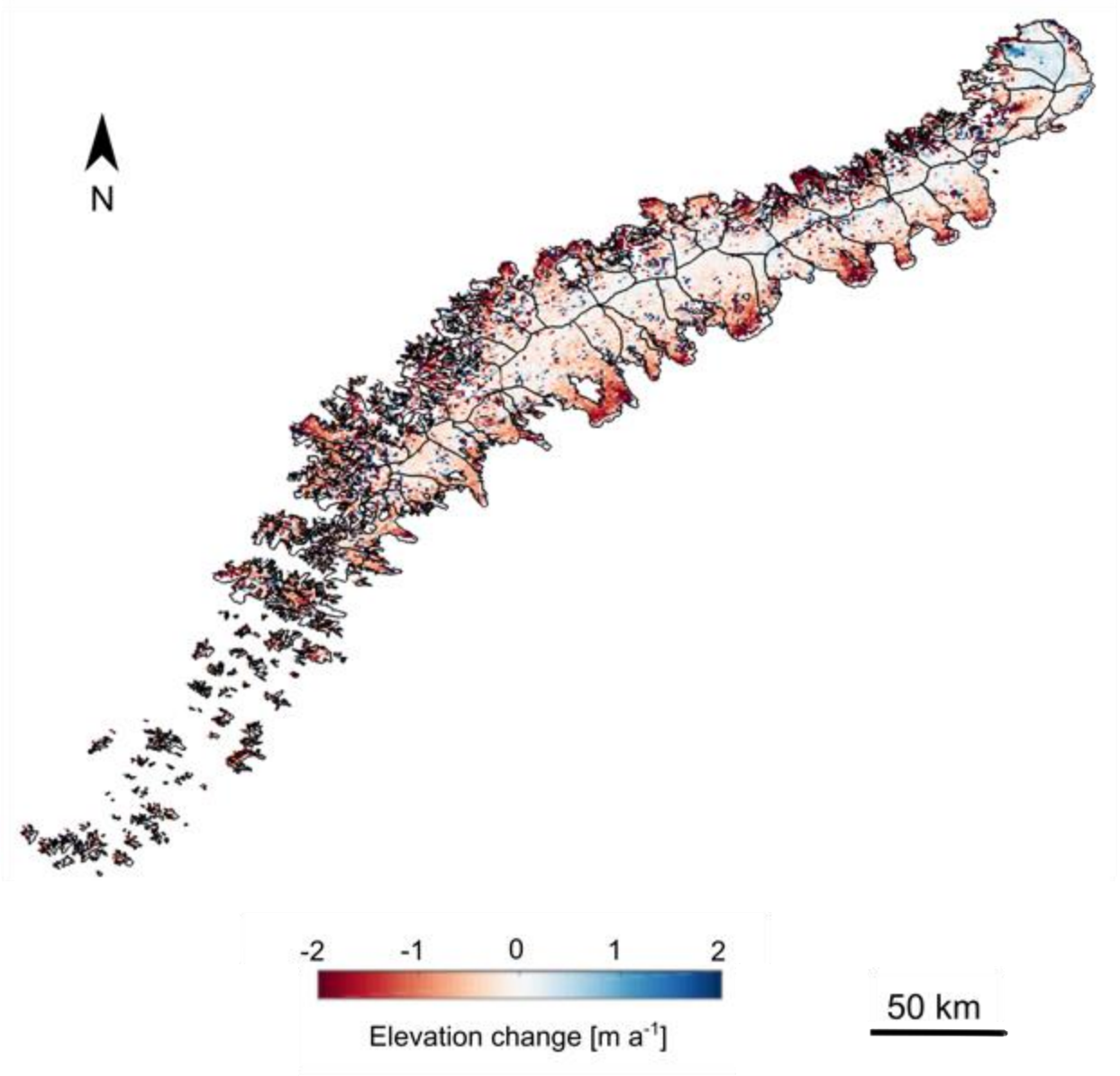

Appendix C4. Surface elevation change rates (2010-2017) over Severnaya Zemlya at 500 x 500 m resolution. Spurious elevation changes removed during the post-processing stage are included in the map.

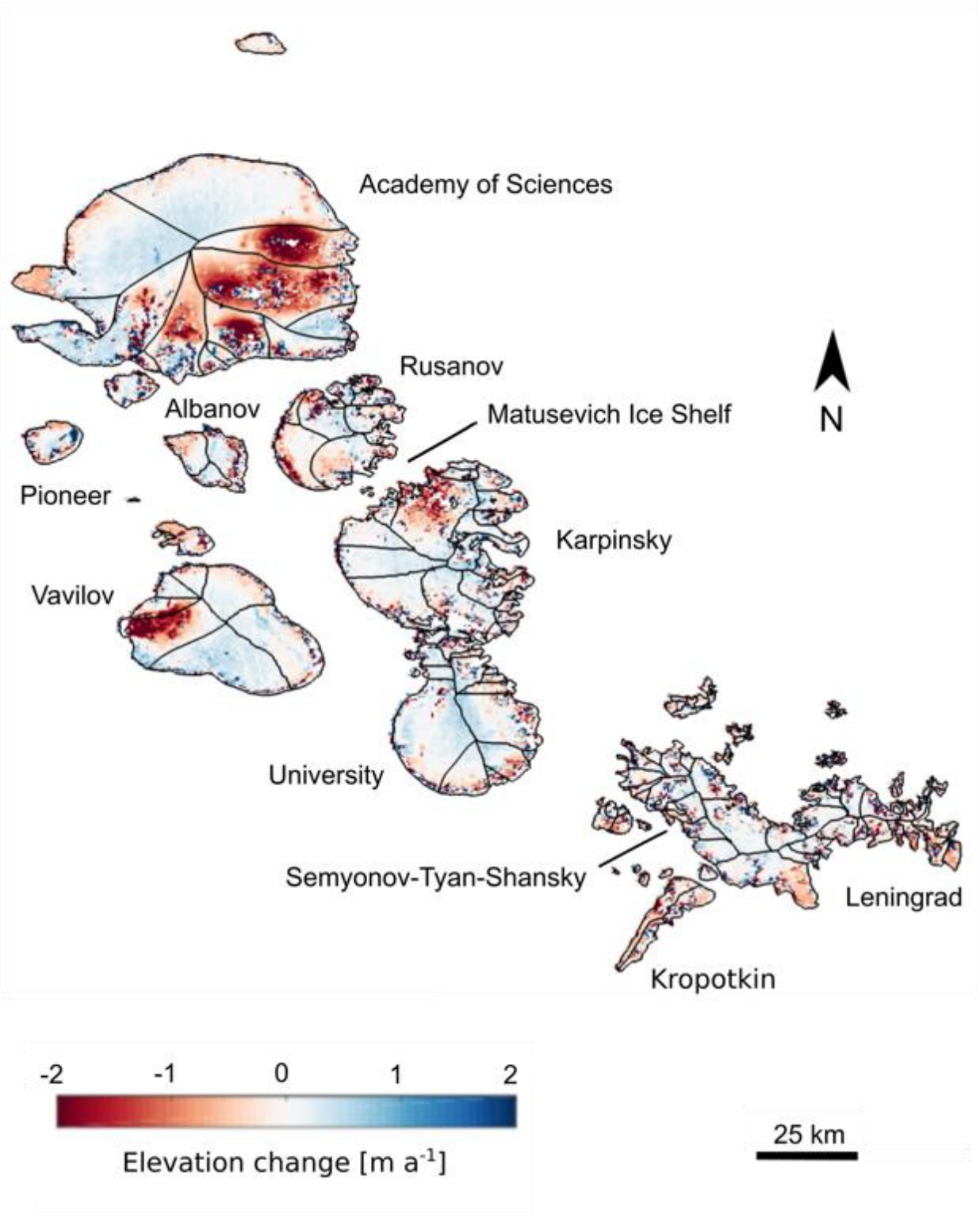

Appendix C5. Surface elevation change rates (2010-2017) over Iceland at 500 x 500 m resolution. Spurious elevation changes removed during the post-processing stage are included in the map.

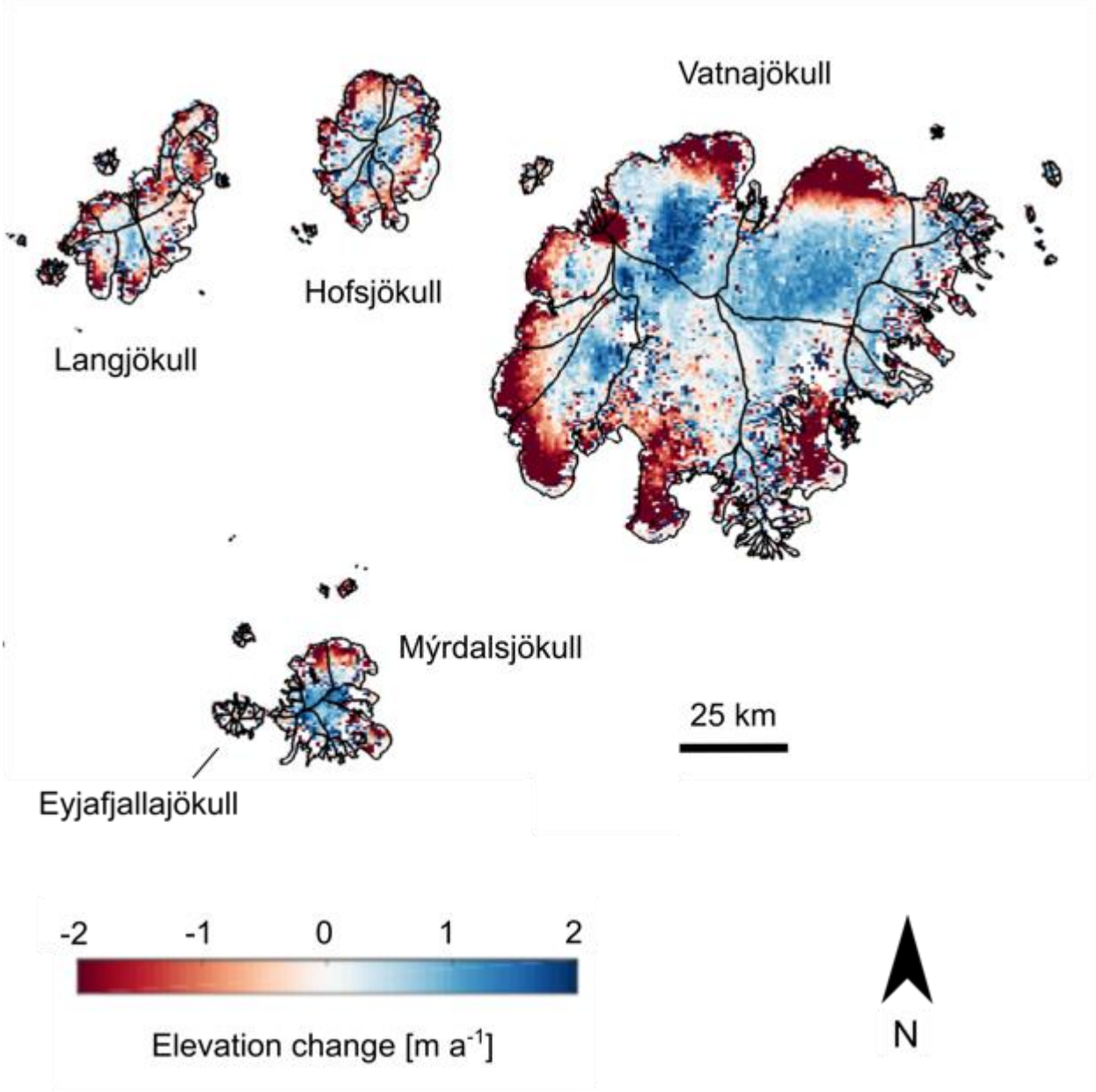

Appendix C6a. Surface elevation change rates (2010-2017) over the Canadian Arctic Archipelagos at 500 x 500 m resolution. Spurious elevation changes removed during the post-processing stage are included in the map.

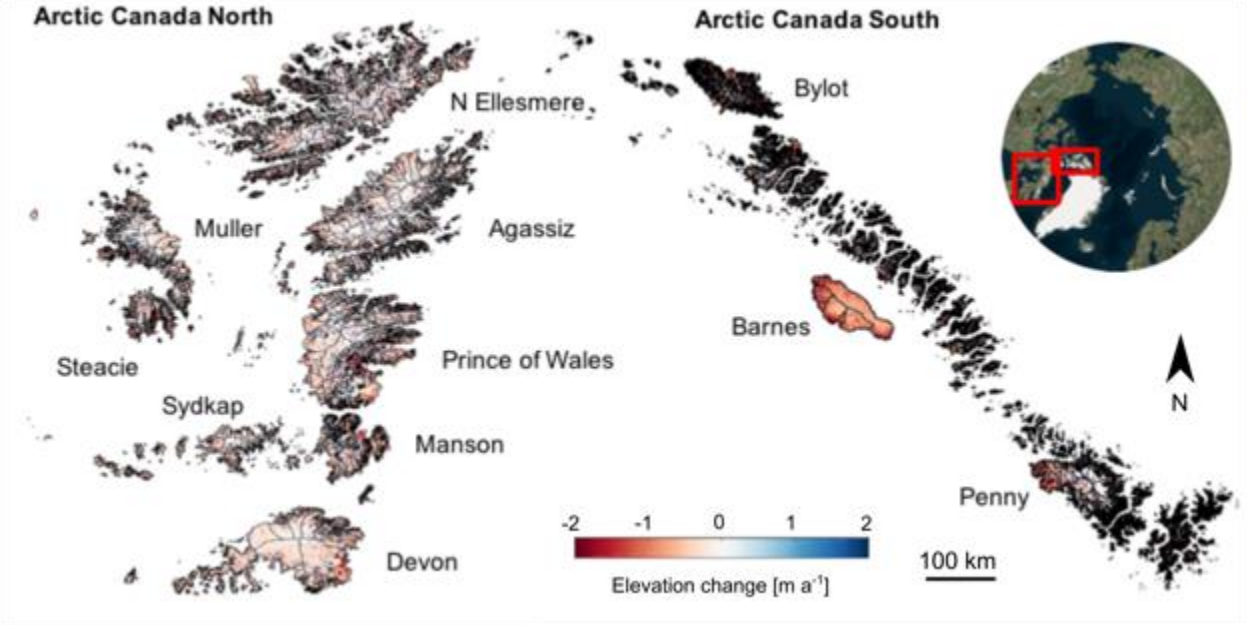

Appendix C6b. Surface elevation change rates (2010-2017) over (a) Bylot Island, (b) Barnes Ice Cap, and (c) Penny Ice Cap, at 500 x 500 m resolution. Spurious elevation changes removed during the post- processing stage are included in the map.

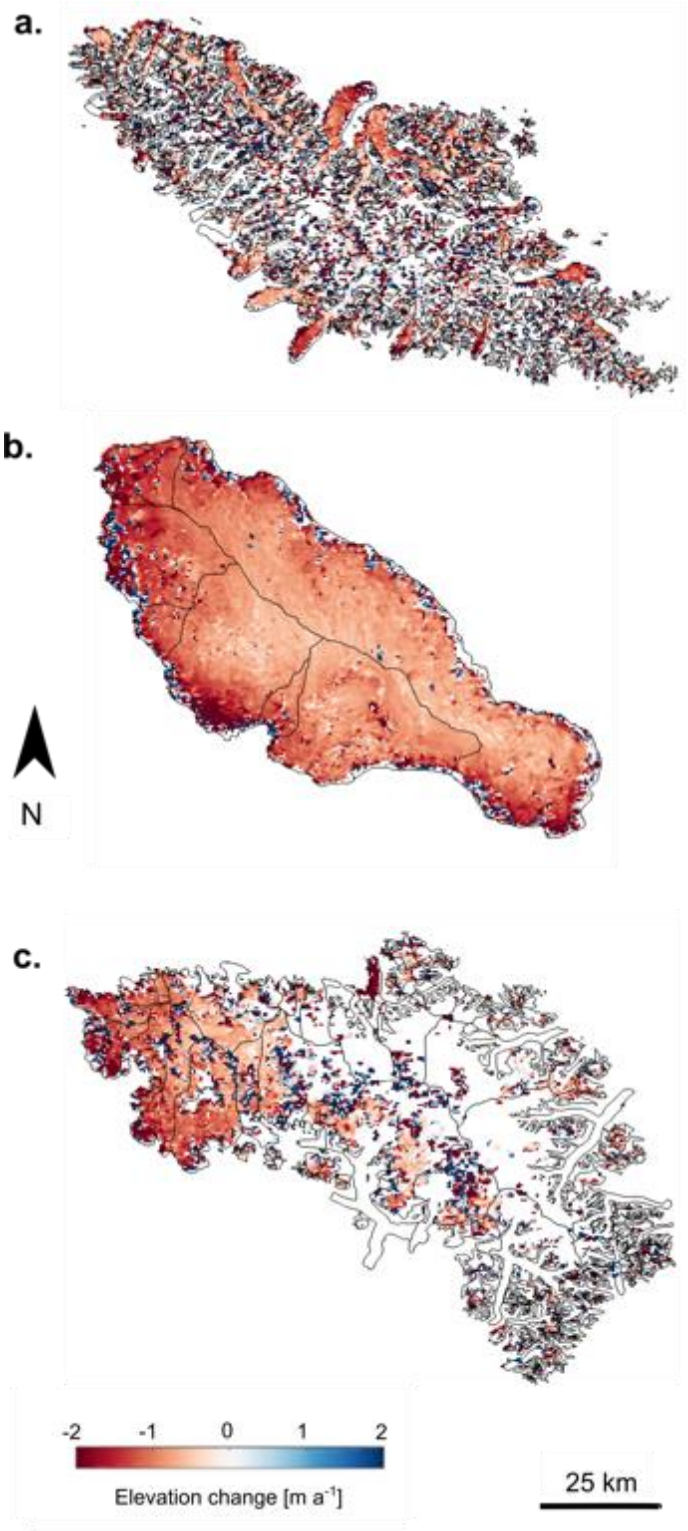

Appendix C6c. Surface elevation change rates (2010-2017) over Devon Ice Cap at 500 x 500 m resolution. Spurious elevation changes removed during the post-processing stage are included in the map.

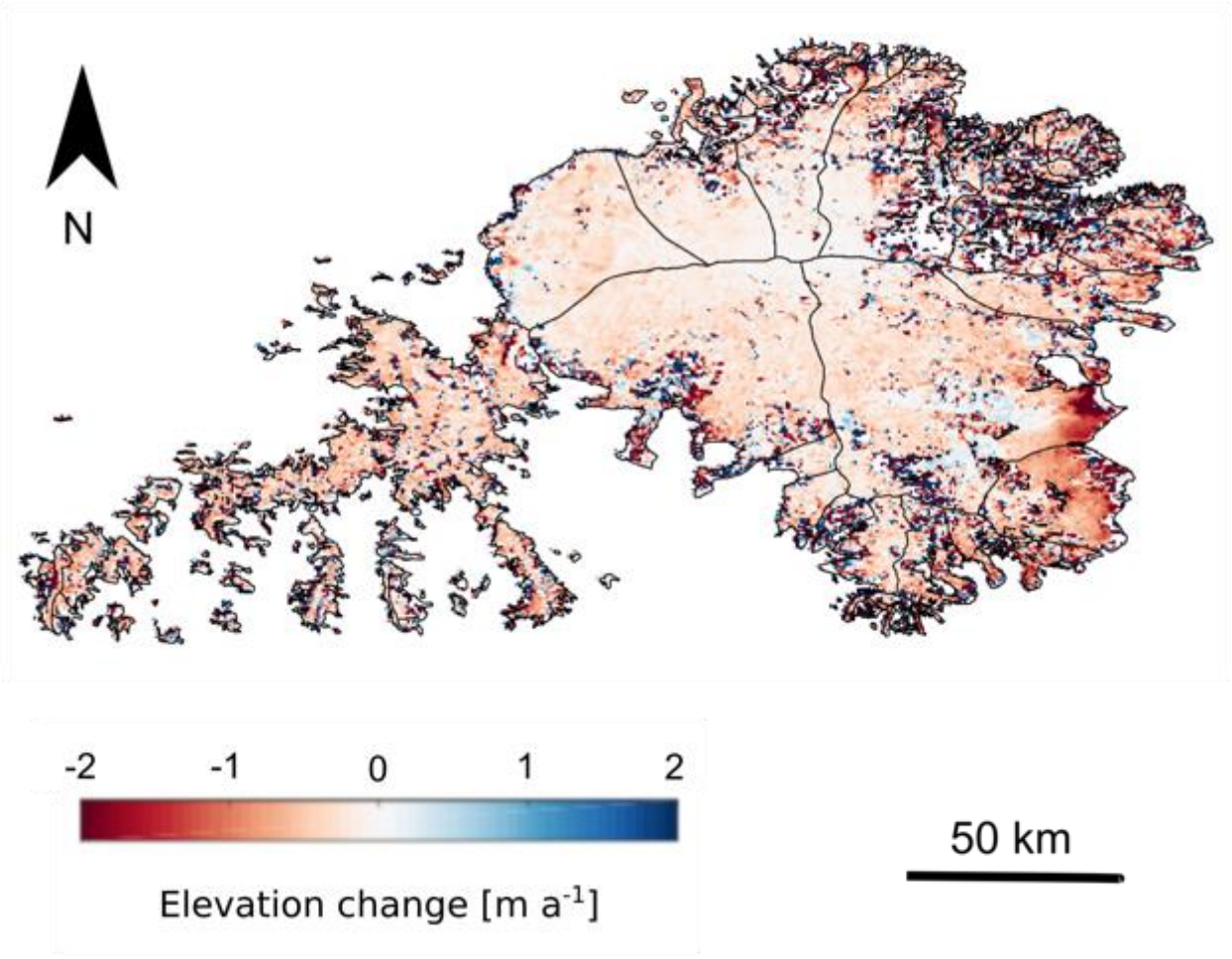

606 **Appendix C6d.** Surface elevation change rates (2010-2017) over (a) Manson and (b) Sydkap Ice
607 Caps at 500 x 500 m resolution. Spurious elevation changes removed during the post-processing
608 stage are included in the map.
609
610

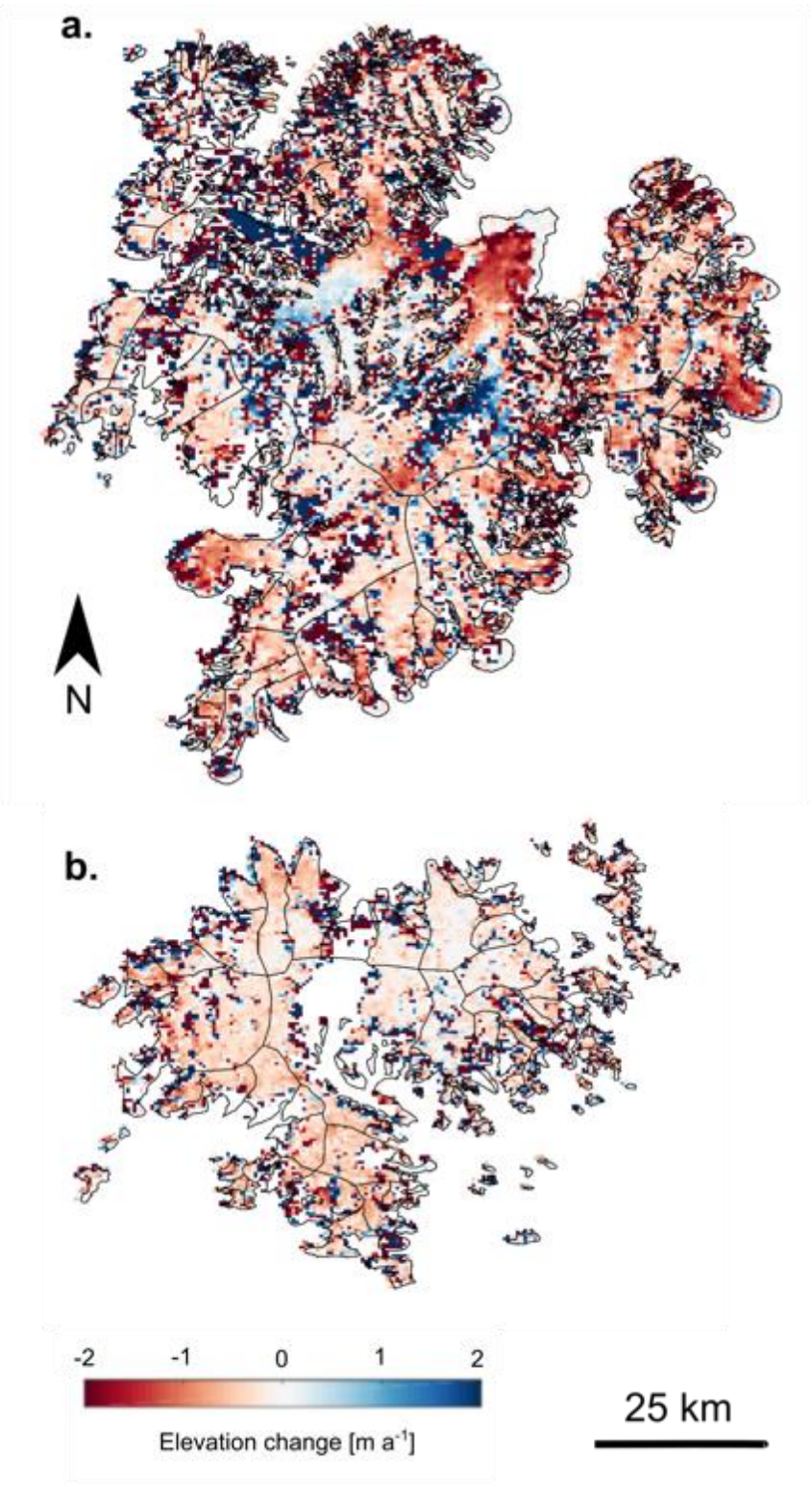

611

Appendix C6e. Surface elevation change rates (2010-2017) over Prince of Wales Ice Field at 500 x 500 m resolution. Spurious elevation changes removed during the post-processing stage are included in the map.

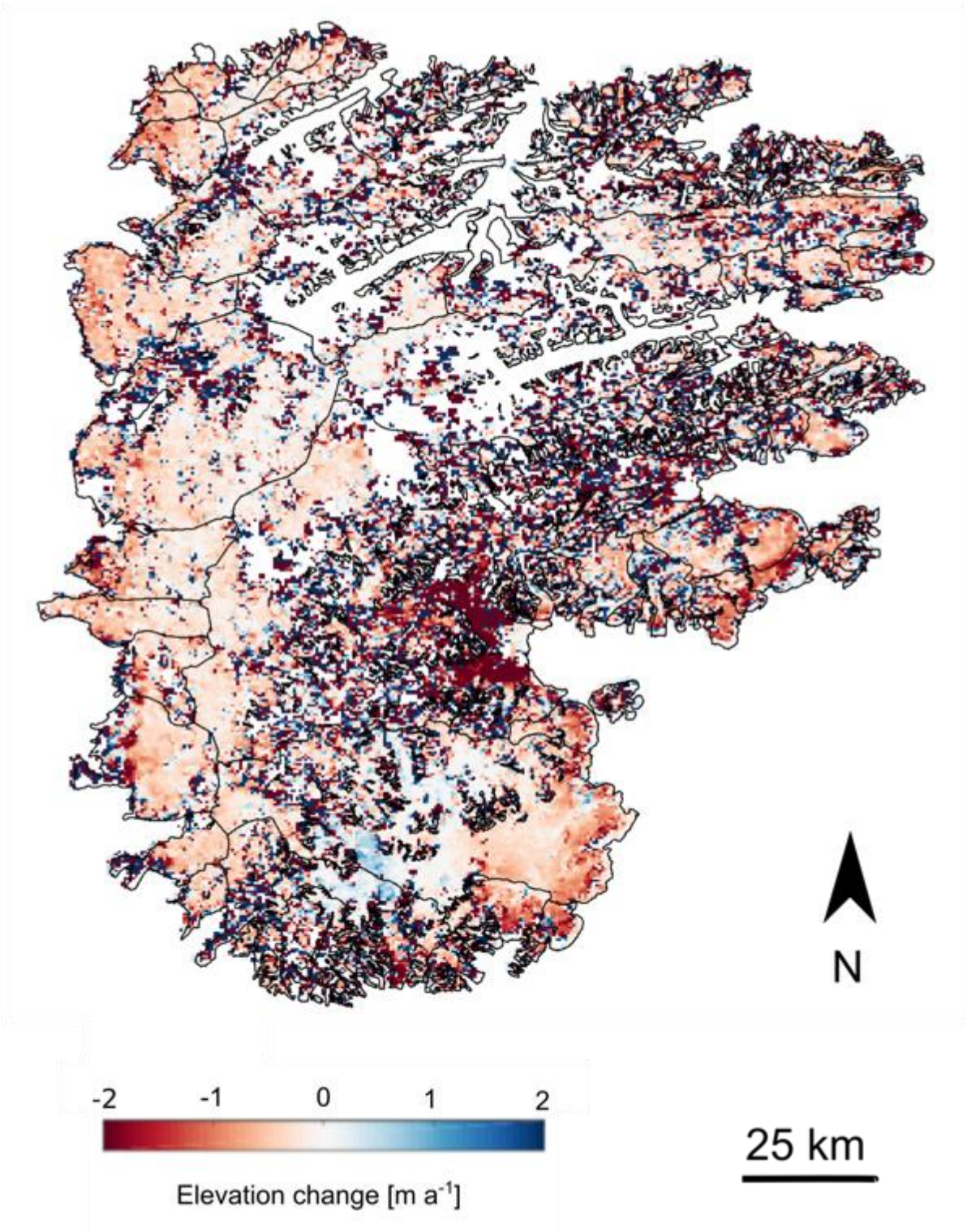

Appendix C6f. Surface elevation change rates (2010-2017) over (a) Muller and (b) Stacie Ice Caps at 500 x 500 m resolution. Spurious elevation changes removed during the post-processing stage are included in the map.

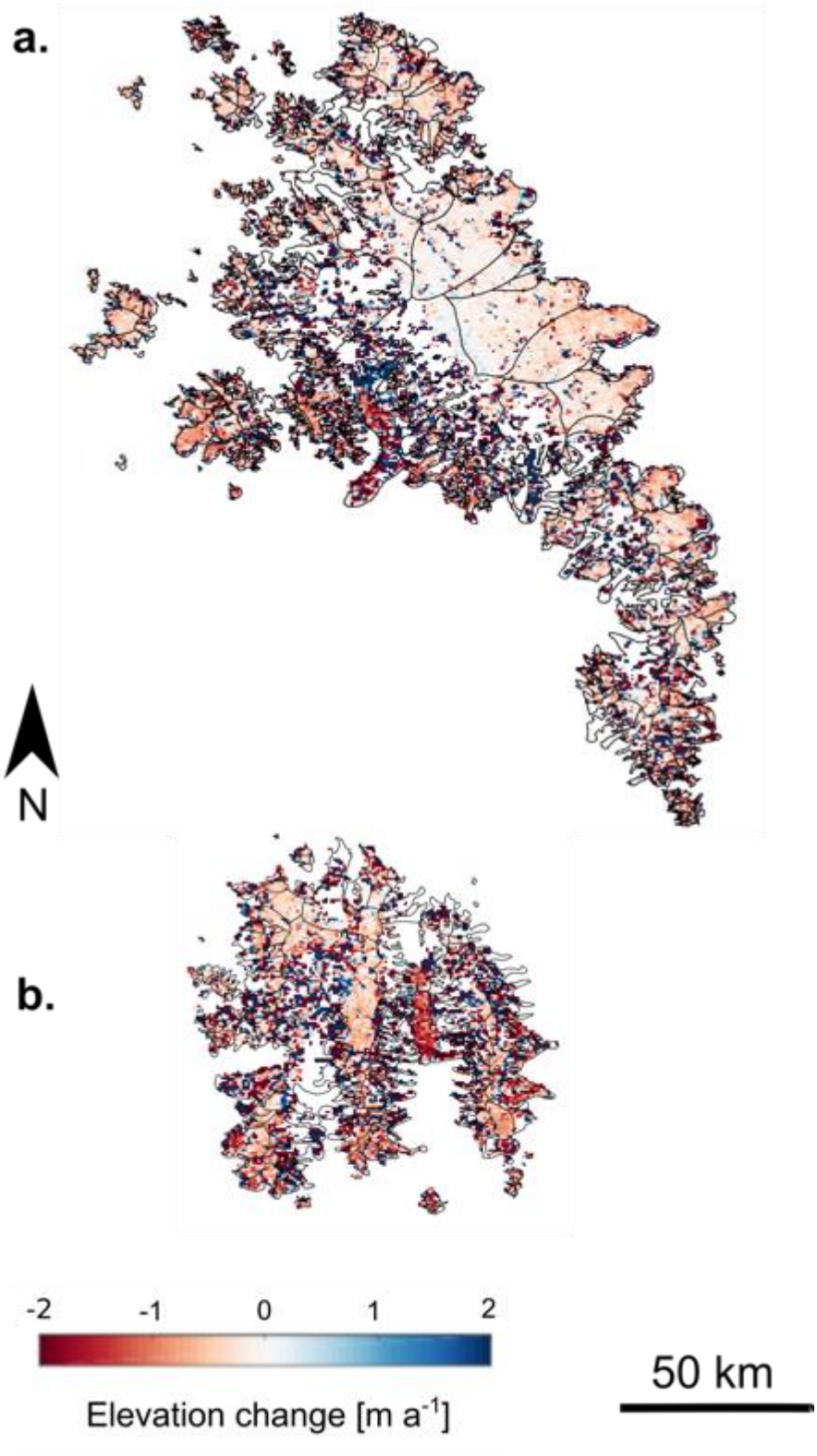

Appendix C6g. Surface elevation change rates (2010-2017) over (a) Northern Ellesmere ice fields and (b) Agassiz Ice Cap at 500 x 500 m resolution. Spurious elevation changes removed during the post-processing stage are included in the map.

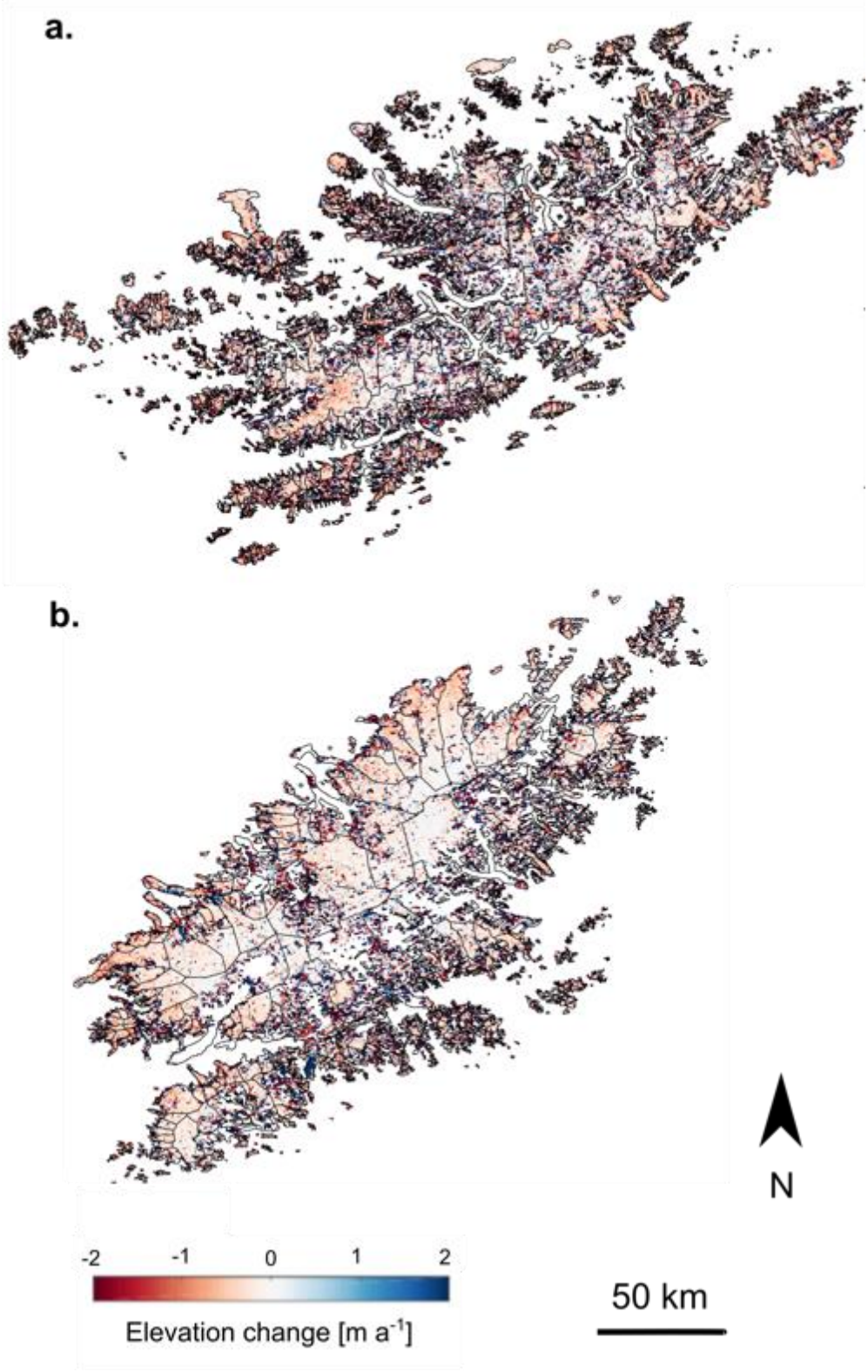

Appendix D. Atmospheric and oceanic forcing anomalies.

T_{2m} decadal anomalies (ERA-Interim). Left: T_{2m} decadal mean of annual means (°C) for the 1990-1999 (baseline) period. **Middle:** T_{2m} anomaly (°C) between 2000-2009 and the baseline period. **Right:** T_{2m} anomaly (°C) between 2010-2017 and 2000-2009.

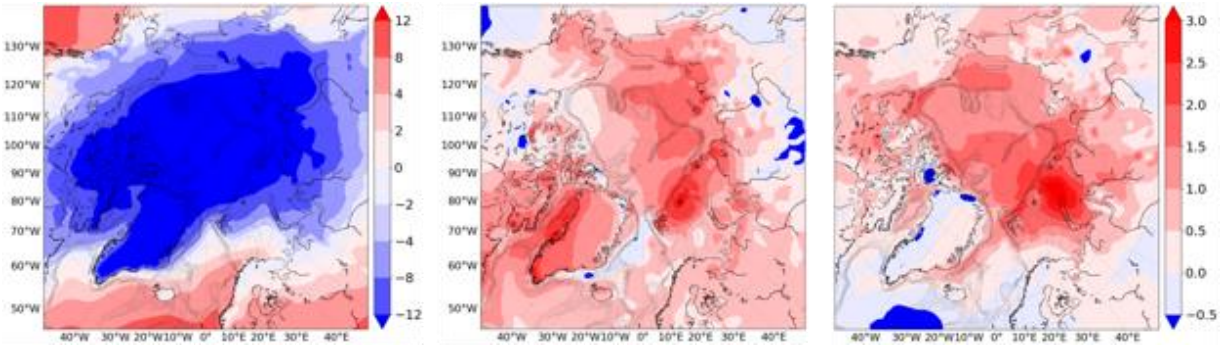

SST decadal anomalies (ERA-Interim). Left: SST decadal mean of annual means (°C) for the 1990-1999 (baseline) period. **Middle:** SST anomaly (°C) between 2000-2009 and the baseline period. **Right:** SST anomaly (°C) between 2010-2017 and 2000-2009.

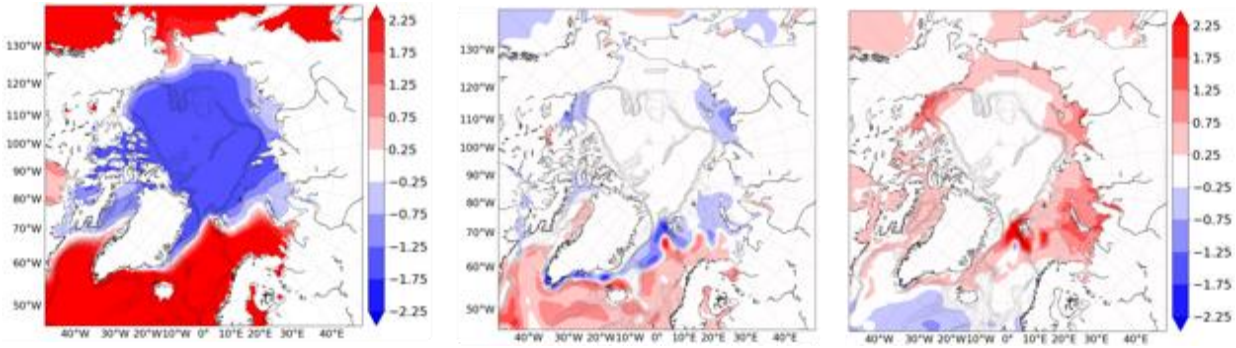

SOT decadal anomalies (TOPAZ). Left: SOT decadal mean of annual means (°C) for the 1990-1999 (baseline) period. **Middle:** SOT anomaly (°C) between 2000-2009 and the baseline period. **Right:** SOT anomaly (°C) between 2010-2017 and 2000-2009.

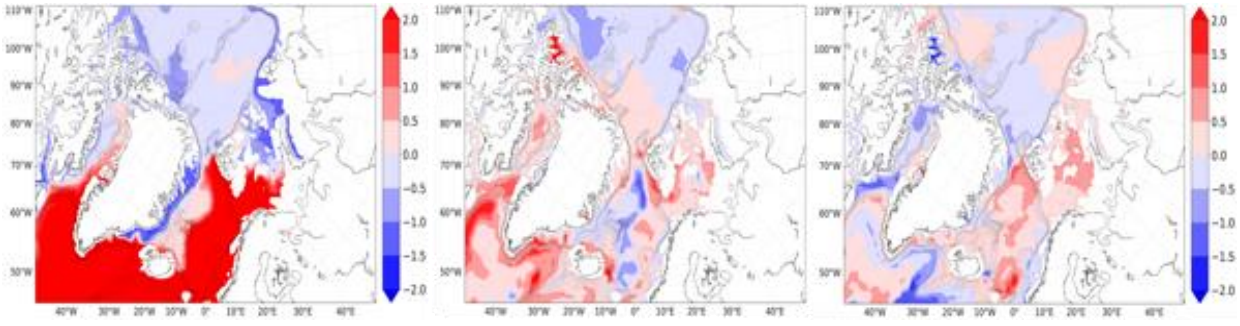

SIC decadal anomalies (NASA Team). Left: SIC decadal mean of annual means (%) for the 1990-1999 (baseline) period. **Middle:** SIC anomaly (%) between 2000-2009 and the baseline period. **Right:** SIC anomaly (%) between 2010-2017 and 2000-2009.

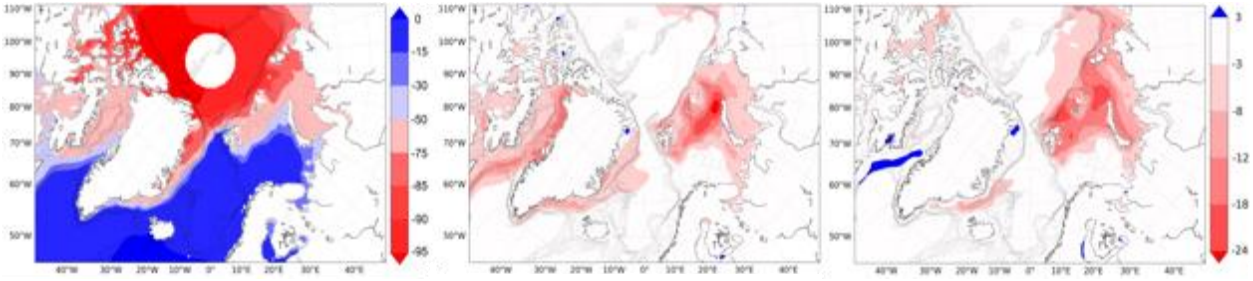

Appendix E. Coverage of surface elevation change $\dot{h}$ along ice margins with extreme topography. Example of Trinity-Wykeham Glacier, Nunavut, Canada. ICESat (left panel) for reference, and CryoSat-2 (right panel). Adapted from Harcourt et al. (2019).

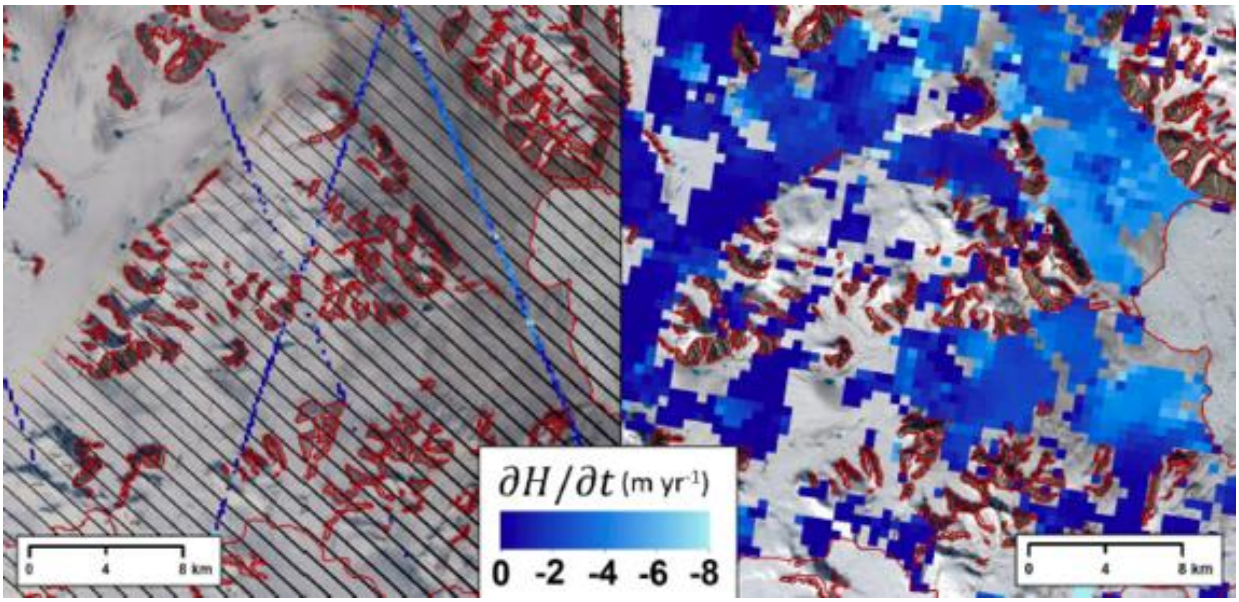

Appendix F. Validation of CryoSat-2 (CS2) rates of elevation change $\dot{h}$ (or dh/dt) against OIB: Barnes Ice Cap (top panels), and the Devon Ice Cap (bottom panels) with differences of 0.05 m $a^{-1} \pm 0.26$ m a^{-1} and 0.00 m $a^{-1} \pm 0.13$ m a^{-1} respectively for Barnes and Devon Ice Caps.

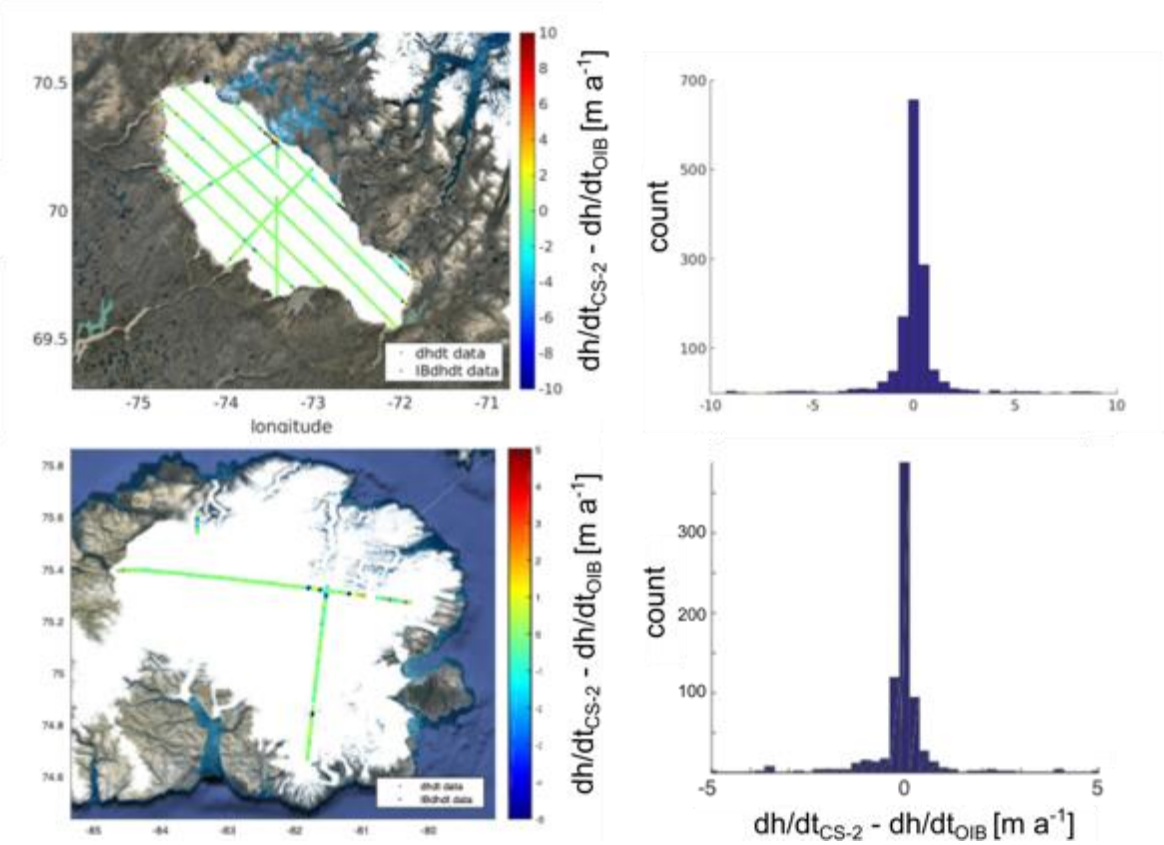

Appendix G. SMB parametrisation coefficients in [10^{-3} a^{-1}]: numbers in brackets for each region indicate the values of lat_ts and lon_0 of the local polar stereographic projection used to calculate the x and y components of the parametrisation of $\dot{h}$.

Region [lat_ts lon_0]	a_0	a_1	a_2	a_3	a_4
FJL [80.5 55.0]	1.7e^{-5}	-1.4e^{-2}	4.5	1.4e^{-3}	2.0e^{-3}
NZ [75.5 61.0]	-2.9e^{-6}	4.2e^{-3}	-0.5	1.7e^{-3}	0.3e^{-3}
SZ [79.5 99.0]	-7.3e^{-7}	-1.6e^{-3}	2.0	-1.0e^{-3}	0.2e^{-3}
Sv [78.5 20.0]	6.3e^{-7}	-2.9e^{-3}	3.8	1.4 e^{-3}	1.6e^{-3}
Ic [65.0 -19.0]	-	-	-	-	-
CAA-N [79.0 -84.0]	-5.3e^{-7}	2.0e^{-3}	-2.0	0.1 e^{-3}	-0.2e^{-3}
CAA-S [70.0 -73.0]	-4.2e^{-7}	1.3e^{-3}	-0.6	4.8 e^{-5}	0.6e^{-3}

References

Barton, B.I., Lenn, Y.-D., Lique, C., 2018. Observed atlantification of the Barents Sea causes the Polar Front to limit the expansion of winter sea ice. J. Phys. Oceanogr. 48, 1849–1866. https://doi.org/10.1175/jpo-d-18-0003.1

Bjørk, A.A., Aagaard, S., Lütt, A., Khan, S.A., Box, J.E., Kjeldsen, K.K., Larsen, N.K., Korsgaard, N.J., Cappelen, J., Colgan, W.T., Machguth, H., Andresen, C.S., Peings, Y., Kjær, K.H., 2018. Changes in Greenland's peripheral glaciers linked to the North Atlantic Oscillation. Nat. Clim. Chang. 8, 48–52. https://doi.org/10.1038/s41558-017-0029-1

Blaszczyk, M., Jania, J.A., Hagen, J.O., 2009. Tidewater glaciers of Svalbard: Recent changes and estimates of calving fluxes, Polish Polar Research.

Byrne, M.P., Schneider, T., 2018. Atmospheric dynamics feedback: concept, simulations and climate implications. J. Clim. 31, 3249–3264. https://doi.org/10.1175/JCLI-D-17-0470.1

Carr, J.R., Bell, H., Killick, R., Holt, T., 2017. Exceptional retreat of Novaya Zemlya's marine-terminating outlet glaciers between 2000 and 2013. Cryosph. 11, 2149–2174. https://doi.org/10.5194/tc-11-2149-2017

Cavalieri, D., Parkinson, C., Gloersen, P., Zwally, J.H., 2019. Sea ice concentrations from Nimbus-7 SMMR and DMSP SSM/I-SSMIS passive microwave data, Version 1. Boulder, Colorado USA.

Christie, F.D.W., Bingham, R.G., Gourmelen, N., Tett, S.F.B., Muto, A., 2016. Four-decade record of pervasive grounding line retreat along the Bellingshausen margin of West Antarctica. Geophys. Res. Lett. 43, 5741–5749. https://doi.org/10.1002/2016GL068972

Church, J.A. et al., 2013. Climate Change 2013: The Physical Science Basis. Contribution of Working Group I to the Fifth Assessment Report of the Intergovernmental Panel on Climate Change (IPCC). Cambridge Univ. Press, Cambridge.

Ciracì, E., Velicogna, I., Sutterley, T.C., 2018. Mass Balance of Novaya Zemlya Archipelago, Russian high arctic, using time-variable gravity from GRACE and altimetry data from ICESat and CryoSat-2. Remote Sens. 10. https://doi.org/10.3390/rs10111817

Ciracì, E., Velicogna, I., Swenson, S., 2020. Continuity of the Mass Loss of the World ' s Glaciers and Ice Caps From the GRACE and GRACE Follow-On Missions. Geophys. Res. Lett. 47, 1–11. https://doi.org/10.1029/2019GL086926

Comiso, J.C., 2017. Bootstrap sea ice concentrations from Nimbus-7 SMMR and DMSP SSM/I-SSMIS, Version 3. Boulder, Colorado USA.

Cook, A.J., Copland, L., Noël, B.P.Y., Stokes, C.R., Bentley, M.J., Sharp, M.J., Bingham, R.G., van den Broeke, M.R., 2019. Atmospheric forcing of rapid marine-terminating glacier retreat in the Canadian Arctic Archipelago. Sci. Adv. 5, 8507. https://doi.org/10.1126/sciadv.aau8507

Cowton, T.R., Sole, A.J., Nienow, P.W., Slater, D.A., Christoffersen, P., 2018. Linear response of east Greenland's tidewater glaciers to ocean/atmosphere warming. Proc. Natl. Acad. Sci. 115, 7907–7912. https://doi.org/10.1073/pnas.1801769115

Cuffey, K.M., Paterson, W.S.B., 2010. The Physics of Glaciers, 4th ed. ed. Elsevier, Amsterdam.

Dee, D.P., Uppala, S.M., Simmons, A.J., Berrisford, P., Poli, P., Kobayashi, S., Andrae, U., Balmaseda, M.A., Balsamo, G., Bauer, P., Bechtold, P., Beljaars, A.C.M., van de Berg, L., Bidlot, J., Bormann, N., Delsol, C., Dragani, R., Fuentes, M., Geer, A.J., Haimberger, L., Healy, S.B., Hersbach, H., Hólm, E. V., Isaksen, L., Kållberg, P., Köhler, M., Matricardi, M., Mcnally, A.P., Monge-Sanz, B.M., Morcrette, J.J., Park, B.K., Peubey, C., de Rosnay, P., Tavolato, C., Thépaut, J.N., Vitart, F., 2011. The ERA-Interim reanalysis: Configuration and performance of the data assimilation system. Q. J. R. Meteorol. Soc. 137, 553–597. https://doi.org/10.1002/qj.828

Delhasse, A., Fettweis, X., Kittel, C., Amory, C., Agosta, C., 2018. Brief communication: Impact

of the recent atmospheric circulation change in summer on the future surface mass balance of the Greenland Ice Sheet. Cryosphere 12, 3409–3418. https://doi.org/10.5194/tc-12-3409-2018
Ding, Q., Wallace, J.M., Battisti, D.S., Steig, E.J., Gallant, A.J.E., Kim, H.-J., Geng, L., 2014. Tropical forcing of the recent rapid Arctic warming in northeastern Canada and Greenland. Nature 509, 209–212. https://doi.org/10.1038/nature13260
Dunse, T., Schellenberger, T., Hagen, J.O., Kääb, A., Schuler, T. V., Reijmer, C.H., 2015. Glacier-surge mechanisms promoted by a hydro-thermodynamic feedback to summer melt. Cryosphere 9, 197–215. https://doi.org/10.5194/tc-9-197-2015
Enderlin, E.M., Howat, I.M., Jeong, S., Noh, M.-J., van Angelen, J.H., van den Broeke, M.R., 2014. An improved mass budget for the Greenland ice sheet. Geophys. Res. Lett. 41, 866–872.
Farinotti, D., Huss, M., Fürst, J.J., Landmann, J., Machguth, H., Maussion, F., Pandit, A., 2019. A consensus estimate for the ice thickness distribution of all glaciers on Earth. Nat. Geosci. 12, 168–173. https://doi.org/10.1038/s41561-019-0300-3
Foresta, L., Gourmelen, N., Pálsson, F., Nienow, P., Björnsson, H., Shepherd, A., 2016. Surface elevation change and mass balance of Icelandic ice caps derived from swath mode CryoSat-2 altimetry. Geophys. Res. Lett. 43, 12138–12145. https://doi.org/10.1002/2016GL071485
Foresta, L., Gourmelen, N., Weissgerber, F., Nienow, P., Williams, J.J., Shepherd, A., Drinkwater, M.R., Plummer, S., 2018. Heterogeneous and rapid ice loss over the Patagonian Ice Fields revealed by CryoSat-2 swath radar altimetry. Remote Sens. Environ. 211, 441–455. https://doi.org/10.1016/j.rse.2018.03.041
Gardner, A.S., Moholdt, G., Arendt, A., Wouters, B., 2012. Accelerated contributions of Canada's Baffin and Bylot Island glaciers to sea level rise over the past half century. Cryosph. 6, 1103–1125. https://doi.org/10.5194/tc-6-1103-2012
Gardner, A.S., Moholdt, G., Cogley, J.G., Wouters, B., Arendt, A. a., Wahr, J., Berthier, E., Hock, R., Pfeffer, W.T., Kaser, G., Ligtenberg, S.R.M., Bolch, T., Sharp, M.J., Hagen, J.O., van den Broeke, M.R., Paul, F., 2013. A reconciled estimate of glacier contributions to sea level rise: 2003 to 2009. Science 340, 852–857. https://doi.org/10.1126/science.1234532
Gardner, A.S., Moholdt, G., Wouters, B., Wolken, G.J., Burgess, D.O., Sharp, M.J., Cogley, J.G., Braun, C., Labine, C., 2011. Sharply increased mass loss from glaciers and ice caps in the Canadian Arctic Archipelago. Nature 473, 357–360. https://doi.org/10.1038/nature10089
Gardner, A.S., Sharp, M., 2006. Influence of the Arctic Circumpolar Vortex on the mass balance of Canadian High Arctic glaciers. J. Clim. 20, 4586–4598. https://doi.org/10.1175/JCLI4268.1
Glazovskiy, A.F., 1996. Mass Balance of Arctic Glaciers, IASC Report No. 5. University of Silesia, Sosnowiec-Oslo, Norway.
Gourmelen, N., Escorihuela, M.J., Shepherd, A., Foresta, L., Muir, A., Garcia-Mondéjar, A., Roca, M., Baker, S.G., Drinkwater, M.R., 2018. CryoSat-2 swath interferometric altimetry for mapping ice elevation and elevation change. Adv. Sp. Res. 62, 1226–1242. https://doi.org/10.1016/j.asr.2017.11.014
Gray, L., Burgess, D., Copland, L., Cullen, R., Galin, N., Hawley, R., Helm, V., 2013. Interferometric swath processing of Cryosat data for glacial ice topography. Cryosphere 7, 1857–1867. https://doi.org/10.5194/tc-7-1857-2013
Gray, L., Burgess, D., Copland, L., Demuth, M.N., Dunse, T., Langley, K., Schuler, T. V., 2015. CryoSat-2 delivers monthly and inter-annual surface elevation change for Arctic ice caps. Cryosph. 9, 1895–1913. https://doi.org/10.5194/tcd-9-2821-2015
Haga, O.N., McNabb, R., Nuth, C., Altena, B., Schellenberger, T., Kääb, A., 2020. From high friction zone to frontal collapse: Dynamics of an ongoing tidewater glacier surge,

Negribreen, Svalbard. J. Glaciol. 66, 742–754. https://doi.org/10.1017/jog.2020.43
Harcourt, W.D., Palmer, S.J., Mansell, D.T., Brocq, A. Le, Bartlett, O., Gourmelen, N., Tepes, P., Dowdeswell, J.A., Donald, D., Young, D.A., Harcourt, W.D., Palmer, S.J., Mansell, D.T., Brocq, A. Le, Bartlett, O., Gourmelen, N., Tepes, P., Dowdeswell, J.A., Blankenship, D.D., 2019. Subglacial controls on dynamic thinning at Trinity- Wykeham Glacier , Prince of Wales Ice Field , Canadian Arctic. Int. J. Remote Sens. 00, 1–23. https://doi.org/10.1080/01431161.2019.1658238
Huss, M., 2013. Density assumptions for converting geodetic glacier volume change to mass change. Cryosph. 7, 877–887. https://doi.org/10.5194/tcd-7-219-2013
Ignéczi, Á., Sole, A.J., Livingstone, S.J., Leeson, A.A., Fettweis, X., Selmes, N., Gourmelen, N., Briggs, K., 2016. Northeast sector of the Greenland Ice Sheet to undergo the greatest inland expansion of supraglacial lakes during the 21st century. Geophys. Res. Lett. 43, 9729–9738. https://doi.org/10.1002/2016GL070338
Labe, Z., Magnusdottir, G., Stern, H., 2018. Variability of Arctic sea ice thickness using PIOMAS and the CESM Large Ensemble. J. Clim. 31, 3233–3247. https://doi.org/10.1175/JCLI-D-17-0436.1
Lind, S., Ingvaldsen, R.B., Furevik, T., 2018. Arctic warming hotspot in the northern Barents Sea linked to declining sea-ice import. Nat. Clim. Chang. 8, 634–639. https://doi.org/10.1038/s41558-018-0205-y
Lindsay, R., Wensnahan, M., Schweiger, A., Zhang, J., 2014. Evaluation of seven different atmospheric reanalysis products in the Arctic*. J. Clim. 27, 2588–2606. https://doi.org/10.1175/JCLI-D-13-00014.1
Martin, T., Adcroft, A., 2010. Parameterizing the fresh-water flux from land ice to ocean with interactive icebergs in a coupled climate model. Ocean Model. 34, 111–124. https://doi.org/10.1016/j.ocemod.2010.05.001
McMillan, M., Shepherd, A., Gourmelen, N., Dehecq, A., Leeson, A., Ridout, A., Flament, T., Hogg, A., Gilbert, L., Benham, T., van den Broeke, M., Dowdeswell, J.A., Fettweis, X., Noel, B., Strozzi, T., 2014. Rapid dynamic activation of a marine-based Arctic ice cap. Geophys. Res. Lett. 41, 8902–8909. https://doi.org/10.1002/2014GL062255
Melkonian, A.K., Willis, M.J., Pritchard, M.E., Stewart, A.J., 2016. Recent changes in glacier velocities and thinning at Novaya Zemlya. Remote Sens. Environ. 174, 244–257. https://doi.org/10.1016/j.rse.2015.11.001
Millan, R., Mouginot, J., Rignot, E., 2017. Mass budget of the glaciers and ice caps of the Queen Elizabeth Islands, Canada, from 1991 to 2015. Environ. Res. Lett. 12, 024016.
Moholdt, G., Heid, T., Benham, T., Dowdeswell, J.A., 2012a. Dynamic instability of marine-terminating glacier basins of Academy of Sciences Ice Cap, Russian High Arctic. Ann. Glaciol. 53, 193–201. https://doi.org/10.3189/2012AoG60A117
Moholdt, G., Nuth, C., Hagen, J.O., Kohler, J., 2010. Recent elevation changes of Svalbard glaciers derived from ICESat laser altimetry. Remote Sens. Environ. 114, 2756–2767. https://doi.org/10.1016/j.rse.2010.06.008
Moholdt, G., Wouters, B., Gardner, A.S., 2012b. Recent mass changes of glaciers in the Russian High Arctic. Geophys. Res. Lett. 39, L10502. https://doi.org/10.1029/2012GL051466
Möller, M., Navarro, F., Martín-Español, A., 2016. Monte Carlo modelling projects the loss of most land-terminating glaciers on Svalbard in the 21st century under RCP 8.5 forcing. Environ. Res. Lett. 11, 094006. https://doi.org/10.1088/1748-9326/11/9/094006
Morris, A., Moholdt, G., Gray, L., 2020. Spread of Svalbard Glacier Mass Loss to Barents Sea Margins Revealed by CryoSat-2. J. Geophys. Res. Earth Surf. 125. https://doi.org/10.1029/2019JF005357
Mortimer, C.A., Sharp, M., Van Wychen, W., 2018. Influence of recent warming and ice dynamics on glacier surface elevations in the Canadian High Arctic, 1995–2014. J. Glaciol.

64, 450–464. https://doi.org/10.1017/jog.2018.37
Mouginot, J., Rignot, E., Bjørk, A.A., van den Broeke, M., Millan, R., Morlighem, M., Noël, B., Scheuchl, B., Wood, M., 2019. Forty-six years of Greenland Ice Sheet mass balance from 1972 to 2018. Proc. Natl. Acad. Sci. 116, 9239–9244. https://doi.org/10.1073/pnas.1904242116
Nick, F.M., Vieli, A., Andersen, M.L., Joughin, I., Payne, A., Edwards, T.L., Pattyn, F., Van De Wal, R.S.W., 2013. Future sea-level rise from Greenland's main outlet glaciers in a warming climate. Nature 497, 235–238. https://doi.org/10.1038/nature12068
Nilsson, J., Gardner, A., Sørensen, L.S., Forsberg, R., 2016. Improved retrieval of land ice topography from CryoSat-2 data and its impact for volume-change estimation of the Greenland Ice Sheet. Cryosphere 10, 2953–2969. https://doi.org/10.5194/tc-10-2953-2016
Nilsson, J., Sørensen, L.S., Barletta, V.R., Forsberg, R., 2015. Mass changes in Arctic ice caps and glaciers: Implications of regionalizing elevation changes. Cryosph. 9, 139–150. https://doi.org/10.5194/tc-9-139-2015
Noël, B., van de Berg, W.J., Lhermitte, S., Wouters, B., Schaffer, N., van den Broeke, M.R., 2018. Six decades of glacial mass loss in the Canadian Arctic Archipelago. J. Geophys. Res. Earth Surf. 123, 1430–1449. https://doi.org/10.1029/2017JF004304
Nuth, C., Gilbert, A., Köhler, A., McNabb, R., Schellenberger, T., Sevestre, H., Weidle, C., Girod, L., Luckman, A., Kääb, A., 2019. Dynamic vulnerability revealed in the collapse of an Arctic tidewater glacier. Sci. Rep. 9, 5541. https://doi.org/10.1038/s41598-019-41117-0
Nuth, C., Moholdt, G., Kohler, J., Hagen, J.O., Kääb, A., 2010. Svalbard glacier elevation changes and contribution to sea level rise. J. Geophys. Res. Earth Surf. 115, 1–16. https://doi.org/10.1029/2008JF001223
Onarheim, I.H., Eldevik, T., Smedsrud, L.H., Stroeve, J.C., 2018. Seasonal and regional manifestation of Arctic sea ice loss. J. Clim. 31, 4917–4932. https://doi.org/10.1175/JCLI-D-17-0427.1
Polyakov, I. V., Pnyushkov, A. V., Alkire, M.B., Ashik, I.M., Baumann, T.M., Carmack, E.C., Goszczko, I., Guthrie, J., Ivanov, V. V., Kanzow, T., Krishfield, R., Kwok, R., Sundfjord, A., Morison, J., Rember, R., Yulin, A., 2017. Greater role for Atlantic inflows on sea-ice loss in the Eurasian Basin of the Arctic Ocean. Science 356, 285–291. https://doi.org/10.1126/science.aai8204
Price, S.F., Payne, A.J., Howat, I.M., Smith, B.E., 2011. Committed sea-level rise for the next century from Greenland ice sheet dynamics during the past decade. Proc. Natl. Acad. Sci. 108, 8978–8983. https://doi.org/10.1073/pnas.1017313108
Radić, V., Bliss, A., Beedlow, A.C., Hock, R., Miles, E., Cogley, J.G., 2014. Regional and global projections of twenty-first century glacier mass changes in response to climate scenarios from global climate models. Clim. Dyn. 42, 37–58. https://doi.org/10.1007/s00382-013-1719-7
Robel, A.A., 2017. Thinning sea ice weakens buttressing force of iceberg mélange and promotes calving. Nat. Commun. 8, 14596. https://doi.org/10.1038/ncomms14596
Sánchez-Gámez, P., Navarro, F.J., Benham, T.J., Glazovsky, A.F., Bassford., R.P., Dowdeswell, J.A., 2019. Intra- and inter-annual variability in dynamic discharge from the Academy of Sciences Ice Cap, Severnaya Zemlya, Russian Arctic, and its role in modulating mass balance. J. Glaciol. 65, 780–797. https://doi.org/10.1017/jog.2019.58
Schuler, T. V., Kohler, J., Elagina, N., Hagen, J.O.M., Hodson, A.J., Jania, J.A., Kääb, A.M., Luks, B., Małecki, J., Moholdt, G., Pohjola, V.A., Sobota, I., Van Pelt, W.J.J., 2020. Reconciling Svalbard Glacier Mass Balance. Front. Earth Sci. 8, 1–16. https://doi.org/10.3389/feart.2020.00156
Shindell, D., Faluvegi, G., 2009. Climate response to regional radiative forcing during the twentieth century. Nat. Geosci. 2, 294–300. https://doi.org/10.1038/ngeo473
Slater, D.A., Goldberg, D.N., Nienow, P.W., Cowton, T.R., 2016. Scalings for submarine melting

at tidewater glaciers from buoyant plume theory. J. Phys. Oceanogr. 46, 1839–1855. https://doi.org/10.1175/jpo-d-15-0132.1

Strozzi, T., Kääb, A., Schellenberger, T., 2017a. Frontal destabilization of Stonebreen, Edgeøya, Svalbard. Cryosphere 11, 553–566. https://doi.org/10.5194/tc-11-553-2017

Strozzi, T., Paul, F., Wiesmann, A., Schellenberger, T., Kääb, A., 2017b. Circum-arctic changes in the flow of glaciers and ice caps from satellite SAR data between the 1990s and 2017. Remote Sens. 9. https://doi.org/10.3390/rs9090947

Studinger, M., 2014. IceBridge ATM L4 Surface Elevation Rate of Change, Version 1. Boulder, Colorado USA. https://doi.org/https://doi.org/10.5067/BCW6CI3TXOCY

Thornalley, D.J.R., Delia, W., Ortega, P., Robson, J.I., Brierley, C.M., Davis, R., Hall, I.R., Moffa-sanchez, P., Rose, N.L., Spooner, P.T., Yashayaev, I., Keigwin, L.D., 2018. Atlantic overturning during the past 150 years. Nature 556, 227–230. https://doi.org/10.1038/s41586-018-0007-4

Willis, M.J., Melkonian, A.K., Pritchard, M.E., 2015. Outlet glacier response to the 2012 collapse of the Matusevich Ice Shelf, Severnaya Zemlya, Russian Arctic. J. Geophys. Res. Earth Surf. 120, 2040–2055. https://doi.org/10.1002/2015JF003544

Willis, M.J., Zheng, W., Durkin, W.J., Pritchard, M.E., Ramage, J.M., Dowdeswell, J.A., Benham, T.J., Bassford, R.P., Stearns, L.A., Glazovsky, A.F., Macheret, Y.Y., Porter, C.C., 2018. Massive destabilization of an Arctic ice cap. Earth Planet. Sci. Lett. 502, 146–155. https://doi.org/10.1016/j.epsl.2018.08.049

Wingham, D.J., Francis, C.R., Baker, S., Bouzinac, C., Brockley, D., Cullen, R., de Chateau-Thierry, P., Laxon, S.W., Mallow, U., Mavrocordatos, C., Phalippou, L., Ratier, G., Rey, L., Rostan, F., Viau, P., Wallis, D.W., 2006. CryoSat: A mission to determine the fluctuations in Earth's land and marine ice fields. Adv. Sp. Res. 37, 841–871. https://doi.org/10.1016/j.asr.2005.07.027

Wouters, B., Gardner, A.S., Moholdt, G., 2019. Global glacier mass loss during the GRACE satellite mission (2002-2016). Front. Earth Sci. 7, 1–11. https://doi.org/10.3389/feart.2019.00096

Xie, J., Bertino, L., Knut, L., Sakov, P., 2017. Quality assessment of the TOPAZ4 reanalysis in the Arctic over the period 1991-2013. Ocean Sci. 13, 123–144. https://doi.org/10.5194/os-13-123-2017

Yang, Q., Dixon, T.H., Myers, P.G., Bonin, J., Chambers, D., Van Den Broeke, M.R., 2016. Recent increases in Arctic freshwater flux affects Labrador Sea convection and Atlantic overturning circulation. Nat. Commun. 7. https://doi.org/10.1038/ncomms10525

Zeeberg, J., Forman, S.L., 2001. Changes in glacier extent on north Novaya Zemlya in the twentieth century. The Holocene 11, 161–175. https://doi.org/10.1191/095968301676173261

Zemp, M., Huss, M., Thibert, E., Eckert, N., McNabb, R., Huber, J., Barandun, M., Machguth, H., Nussbaumer, S.U., Gärtner-Roer, I., Thomson, L., Paul, F., Maussion, F., Kutuzov, S., Cogley, J.G., 2019. Global glacier mass changes and their contributions to sea-level rise from 1961 to 2016. Nature 568, 382–386. https://doi.org/10.1038/s41586-019-1071-0

Zheng, W., Pritchard, M.E., Willis, M.J., Stearns, L.A., 2019. The Possible Transition From Glacial Surge to Ice Stream on Vavilov Ice Cap. Geophys. Res. Lett. 46, 13892–13902. https://doi.org/10.1029/2019GL084948

Zheng, W., Pritchard, M.E., Willis, M.J., Tepes, P., Gourmelen, N., Benham, T.J., Dowdeswell, J.A., 2018. Accelerating glacier mass loss on Franz Josef Land, Russian Arctic. Remote Sens. Environ. 211, 357–375.

List of Figure Captions

Fig. 2. Rates of $\dot{h}$ (expanded maps available in Appendices C1-C6), glaciated area of marine- and land-terminating glacier catchments, and Arctic GIC mass balance represented in graphical form as boxes indicating average values over their respective study period (width) with error estimates (height). A map of the Arctic shows the location of GIC and mass balance from the present study represented by circles with size proportional to the mass losses and their width proportional to the error budget.

Fig. 2. a. CryoSat-2 derived $\dot{h}$ (left) versus RACMO2.3 SMB (right) over Bylot Island, CAA-S; **b.** SMB from CryoSat-2 versus RACMO2.3 across the Canadian Arctic: all regions (red), land-terminating sectors (yellow), marine-terminating sectors (blue); **c.** dynamic thinning $\dot{h} - \dot{h}_{p_m}$ (Appendix A8) over major BKS flow units: Austfonna Ice Cap (upper panel) and Severnaya Zemlya archipelago (lower panel). The white dashed lines demarcate areas of dynamic thinning.

Fig. 3. Area-specific mass balance in [kg m^{-2} a^{-1}]: SMB (orange, left) and D (cyan, right), derived from CryoSat-2. Circles with size proportional to ice mass losses and their width proportional to the corresponding error budget.

Fig. 4. Arctic climate forcing anomalies. Air surface temperature (T_{2m}), sea surface temperature (SST), subsurface ocean temperature (SOT), and sea ice concentration (SIC) anomalies during the CryoSat-2 period (2010-2017) with reference to the baseline period (1990-1999). Anomalies with reference to the previous decade (2000-2009) are provided in Appendix D.

Table 2
Summary table of mass budget: total mass balance and cumulative contributions to sea level rise (SLR) of Arctic GIC from 2010 to 2017.

* Total glaciated area (RGI 6.0), ** mass budgets using a constant density of ice equal to 900 kg m^{-3} (Gardner et al., 2013) for RAA, Sv, Ic, CAA-N and CAA-S, and (Moholdt et al., 2012b) for NZ, SZ and FJL, which cover the period 2004–2009), *** mass budgets using a constant density of ice at 850 kg m^{-3} (900 kg m^{-3} for comparison with the 2003-2009 mass budget estimates).

Table 2
Summary table of D: the dynamic mass budget is calculated with a constant density of ice equal to 850 kg m^{-3}. Area-specific D is computed relative to the total marine-terminating basin area (*) and relative to the total glaciated area (**) of each region. The last column refers to D as a percentage of total mass balance ($\dot{m}$).

Table 3
Anomalies in air surface temperature (T_{2m}), sea surface temperature (SST), subsurface ocean temperature (SOT), and sea ice concentration (SIC) during the survey period (2010-2017) relative to the previous decade (2000-2009). T_{2m} and SST are from ERA-Interim; SOT is 200m depth ocean temperature from TOPAZ; SIC data are from NASA Team/ bootstrap sea ice algorithm (Appendix A11).

Appendix B. Mass balance of Arctic GIC. Split by type of basin (marine- and land-terminating), comparison of upscaling (S) *versus* hypsometric averaging (H) as regionalisation schemes of

land-terminating basins. $A_{measured}$ refers to the proportion (as a percentage) of the total GIC area that has reliable observations after the removal of spurious data points.

Appendix C1. Surface elevation change rates (2010-2017) over Svalbard at 500 x 500 m resolution. Spurious elevation changes removed during the post-processing stage are included in the map.

Appendix C2. Surface elevation change rates (2010-2017) over Franz Josef Land at 500 x 500 m resolution. Spurious elevation changes removed during the post-processing stage are included in the map.

Appendix C3. Surface elevation change rates (2010-2017) over Novaya Zemlya at 500 x 500 m resolution. Spurious elevation changes removed during the post-processing stage are included in the map.

Appendix C4. Surface elevation change rates (2010-2017) over Severnaya Zemlya at 500 x 500 m resolution. Spurious elevation changes removed during the post-processing stage are included in the map.

Appendix C5. Surface elevation change rates (2010-2017) over Iceland at 500 x 500 m resolution. Spurious elevation changes removed during the post-processing stage are included in the map.

Appendix C6a. Surface elevation change rates (2010-2017) over the Canadian Arctic Archipelagos at 500 x 500 m resolution. Spurious elevation changes removed during the post-processing stage are included in the map.

Appendix C6b. Surface elevation change rates (2010-2017) over (a) Bylot Island, (b) Barnes Ice Cap, and (c) Penny Ice Cap, at 500 x 500 m resolution. Spurious elevation changes removed during the post- processing stage are included in the map.

Appendix C6c. Surface elevation change rates (2010-2017) over Devon Ice Cap at 500 x 500 m resolution. Spurious elevation changes removed during the post-processing stage are included in the map.

Appendix C6d. Surface elevation change rates (2010-2017) over (a) Manson and (b) Sydkap Ice Caps at 500 x 500 m resolution. Spurious elevation changes removed during the post-processing stage are included in the map.

Appendix C6e. Surface elevation change rates (2010-2017) over Prince of Wales Ice Field at 500 x 500 m resolution. Spurious elevation changes removed during the post-processing stage are included in the map.

Appendix C6f. Surface elevation change rates (2010-2017) over (a) Muller and (b) Stacie Ice Caps at 500 x 500 m resolution. Spurious elevation changes removed during the post-processing stage are included in the map.

Appendix C6g. Surface elevation change rates (2010-2017) over (a) Northern Ellesmere ice fields and (b) Agassiz Ice Cap at 500 x 500 m resolution. Spurious elevation changes removed during the post-processing stage are included in the map.

Appendix D. Atmospheric and oceanic forcing anomalies.

T_{2m} decadal anomalies (ERA-Interim). Left: T_{2m} decadal mean of annual means (°C) for the 1990-1999 (baseline) period. **Middle:** T_{2m} anomaly (°C) between 2000-2009 and the baseline period. **Right:** T_{2m} anomaly (°C) between 2010-2017 and 2000-2009.

SST decadal anomalies (ERA-Interim). Left: SST decadal mean of annual means (°C) for the 1990-1999 (baseline) period. **Middle:** SST anomaly (°C) between 2000-2009 and the baseline period. **Right:** SST anomaly (°C) between 2010-2017 and 2000-2009.

SOT decadal anomalies (TOPAZ). Left: SOT decadal mean of annual means (°C) for the 1990-1999 (baseline) period. **Middle:** SOT anomaly (°C) between 2000-2009 and the baseline period. **Right:** SOT anomaly (°C) between 2010-2017 and 2000-2009.

SIC decadal anomalies (NASA Team). Left: SIC decadal mean of annual means (%) for the 1990-1999 (baseline) period. **Middle:** SIC anomaly (%) between 2000-2009 and the baseline period. **Right:** SIC anomaly (%) between 2010-2017 and 2000-2009.

Appendix E. Coverage of surface elevation change $\dot{h}$ along ice margins with extreme topography. Example of Trinity-Wykeham Glacier, Nunavut, Canada. ICESat (left panel) for reference, and CryoSat-2 (right panel). Adapted from Harcourt et al. (2019).

Appendix F. Validation of CryoSat-2 (CS2) rates of elevation change $\dot{h}$ (or dh/dt) against OIB: Barnes Ice Cap (top panels), and the Devon Ice Cap (bottom panels) with differences of 0.05 m $a^{-1} \pm 0.26$ m a^{-1} and 0.00 m $a^{-1} \pm 0.13$ m a^{-1} respectively for Barnes and Devon Ice Caps.

Appendix G. SMB parametrisation coefficients in [10^{-3} a^{-1}]: numbers in brackets for each region indicate the values of lat_ts and lon_0 of the local polar stereographic projection used to calculate the x and y components of the parametrisation of $\dot{h}$.